

A closed-loop model of mechanosensation in cells with primary cilia

Wei He¹, Biao Wang¹, Tomasz Boczek^{1,2}, Michael S. Kapiolloff¹, Yang Sun^{1,3,*}

¹ Department of Ophthalmology, Stanford University School of Medicine,

1651 Page Mill Road, Palo Alto, CA 94305, USA

² Department of Molecular Neurochemistry, Medical University of Lodz, 92215, Lodz, Poland

³ Palo Alto Veterans Administration, Palo Alto, CA 94304, US

*Correspondence: Yang Sun: yangsun@stanford.edu

Abstract

The primary cilium is a sensory organelle that mediates perceptions of vision, smell, and laminar flow. The classic mechanosensation model postulates that ciliary ion channels open and cause a cytosolic calcium rise when cilia are bent. However, later experiments proved that calcium does not enter cells through cilia, and how cells detect the flow is still enigmatic. Here we report a branched actin mesh that is unique to ciliated cells and exerts a centrifugal force that excludes ciliary trafficking vesicles from the ciliary base. We demonstrate that the actin mesh, gelsolin, and calcium signaling constitute a closed-loop control system that enables rapid and sustained mechanical transduction from the flow to ciliary signaling. Modulation of this actin mesh restores defective ciliary trafficking of the hedgehog receptor, smoothened, in diseased cells. We anticipate that our study will elucidate the role of primary cilia in many fundamental mechanical force-controlled proliferation and differentiation pathways.

Introduction

Mechanical forces are fundamental regulators of cell differentiation, turnover, shape, and size¹⁻³. Nevertheless, how cells sense and transduce physical force is still not well-understood⁴. The primary cilium is a non-motile, microtubule-based organelle that contains abundant membrane receptors critical to cell differentiation and tissue homeostasis⁵⁻⁷. Cells assemble primary cilia when not in mitosis^{8,9} and, after ciliation, respond to fluid flow with an increase in intracellular calcium¹⁰⁻¹³. Accumulating evidence supports the mechanosensory role of primary cilia after calcium ion channels linked to polycystic kidney disease (PKD) were found on the ciliary membrane^{5, 14, 15}, and the same ion channels were reported to sense the nodal flow in establishing left-right asymmetry in early embryos¹⁶⁻¹⁸.

A classic model of mechanosensation by primary cilia is based on a similar pattern as in signaling models of ciliary G-protein coupled receptors (GPCRs) such as olfactory receptor, rhodopsin and smoothened⁵. Fluid flow bends the cilia causing similar effects as ligand binding to the GPCR, and thus equates the influx of calcium to the activation of an effector protein. However, later experiments reported that controlled bending of the cilia did not induce calcium rise in the cytosol¹⁹. This finding indicates that mechanosensation by primary cilia occurs by a different mechanism than GPCRs, but no further progress has been made in addressing this question.

In studying the influence of fluid flow on ciliary protein trafficking, we report that a centrifugal force drives a collective exclusion of ciliary trafficking vesicles from the cilia. We find that a branched actin structure that encompasses the ciliary base generates this force, exerts the exclusion and adapts the force to the extracellular flow. We then demonstrate a phenotype of stagnated actin

turnover and abnormal flow sensation in diseased cells obtained from a congenital glaucoma mouse model and restore the trafficking of smoothened to the primary cilia by rescuing the actin dynamics with the actin severing protein gelsolin. Lastly, we propose a closed-loop model of mechanosensation in ciliated cells, in which we summarize the flow evoked responses of actin dynamics that are modulated by a feedback sensor.

Results

Collective exclusion of ciliary trafficking vesicles

Here we report single vesicle tracking results obtained from three ciliary membrane proteins: smoothened (SMO), ADP-ribosylation factor-like proteins 13B (ARL13B) and Rab8 (Fig.1, Extended Data Fig. 1,2). We identified a large number of cargo vesicles and cilia in the single color channel within the thickness of a ~400 nm focus plane covering the ciliary base (Fig.1a-c, Supplemental video 1). To follow them simultaneously, we designed a custom MATLAB program based on a previous tracking algorithm for multiple single particles²⁰ (Methods). We found that trajectory patterns differ in cells with and without primary cilia (Fig. 1d, e). In non-ciliated cells the movements of tagged Rab8 vesicles are localized to the cell periphery (Fig. 1d). In contrast, in ciliated cells, their long-range movements extend from the cell periphery to the cilia. Fig. 1e illustrates two different features of the long-range transport of Rab8 labeled vesicles. One group (red, later referred to as Type 1) contains a straight linear pattern of movements to the cilia, as commonly seen in microtubule-based transport^{21, 22}. This pattern is confirmed by the linearly directed microtubule structures in the corresponding region (Fig. 1f). The other group (blue, Type 2) contains trajectories that are zigzag in shape and directed away from the cilia.

Most of the ciliary trafficking vesicles with linear trajectories exhibited Type 2 transport pattern (Fig. 1g). To clarify the direction of vesicle movements, we plotted the distance-time graphs for all trajectories toward and away from the cilia (Fig. 1h, i). In these plots, the distance \mathbf{r} is defined as the length between the vesicle's current location and the ciliary base. The collective rightward-skewed slopes demonstrated that most vesicles are transported outwards. Even the Type 1 vesicles occur in significant displacements in fragments moving toward the cilia (Fig. 1h, arrows) among the collective rightward-skewed small displacements moving away from cilia. This collective exclusion of ciliary trafficking vesicles is not seen in the non-ciliated cells (Fig. 1j).

To explore the origin of the type 2 transport trajectories from cortical actin, we have plotted the histogram of the instant displacement for all linear trajectories selected by aspect ratio (AR < 0.5). Fig. 11 shows the probability of density function (PDF) $P(\Delta r')$ of the instantaneous displacement of the $\Delta r(\tau)$ in duration of $\tau = 7.5$ s, as a function of the normalized variables $\Delta r' = \Delta r/(4D_L\tau)^{1/2}$, where $(4D_L\tau)^{1/2}$ is the average diffusion length, and D_L is the longtime diffusion coefficient of all linear vesicles (Fig. 1k). Instantaneous displacement of the ciliary trafficking vesicles $\Delta r(\tau)$ generated a broad distribution. This distribution also showed a decreased displacement towards the cilia for the Type 2 vesicles (blue) compared to all linear ones (black). This feature of dynamic heterogeneity indicates that the diverse range of the instantaneous displacement may originate from active remodeling activities of cortical actin²⁰.

A branched actin mesh generates the centrifugal force

Positive regulators of branched actin have been reported to decrease ciliogenesis and ciliary length²³⁻²⁵. Branched actin is also known for its motor properties that generate and adapt force²⁶,

²⁷. To identify the origin of the centrifugal force that excludes the ciliary trafficking vesicles, we carefully examined the branched actin labeled by the calponin homology domain of utrophin (UtrCH)²⁸⁻³⁰ in human retinal pigmented epithelial (hRPE1) cells and mouse embryonic fibroblasts (MEFs). We found a unique actin structure at the base of the cilia that is depleted into an ultra-thin mesh that exhibits considerable differences in the mesh sizes and has a high single-fiber turnover rate (~1-3s) (Fig.2a, Extended Data Fig. 3a,b,d, Supplemental video 2). This actin mesh is less well visualized by the commonly used live-cell actin marker, Lifeact³¹, or by the fixed actin marker, phalloidin (Extended Data Fig. 3c, e), and is only found in cells that possess primary cilia (Fig. 2a).

We named the newly identified actin structure, depleted & dynamic actin mesh (DDAM). The depleted feature is more pronounced in the cross-sectional view of the cell than in others and is confirmed by the distribution of the actin-binding protein, Ezrin (Fig. 2b). Single actin filaments exhibit high turnover rates. The polymerization and depolymerization of these actin fibers retain a broad-sized distribution of the mesh. The rapid turnover and large size distribution of the mesh sizes fits the dynamic heterogeneity that we measured (Fig. 1l). To further test whether DDAM produces the centrifugal force, we depleted F-actin with Latrunculin B³². The resulting destruction of DDAM dramatically changed location (Fig. 2c), trajectory pattern (Fig. 2d), and collective exclusion behaviors (Fig. 2e) of the ciliary trafficking vesicles. The direction and distribution of their instantaneous displacement $\Delta r(\tau)$ became randomly distributed (Fig. 1f, g). Measurements from 12 cells also revealed that the cilia length increased from $6.19 \pm 3.27 \mu\text{m}$ to $10.12 \pm 4.30 \mu\text{m}$. Taken together, the results of our experiment showed that DDAM generated the centrifugal force that negatively controlled the ciliary trafficking.

Dynamic responses of DDAM to mechanical and calcium signals demonstrate feedback sensing

To examine the flow response of DDAM, we tested ciliated cells in a laminar flow chamber (see Methods). DDAM immediately increased its fluorescence intensity upon a mild flow stimulation (Fig. 3a, Supplemental video 3). The increasing intensity of DDAM was dependent on flow and dropped rapidly after flow ceased. Remarkably, we observed that cells had significantly large (Fig. 3b, red and green solid curve) as well as mild (Fig. 3b, black and green solid curve) decreases of their fluorescence intensity during this period of flow. Non-ciliated cells also showed an increase when flow was turned on, yet this increase stopped long before the flow ceased and the amplitude was much smaller than in the ciliated cells (Fig. 3b, c).

Measurements of the rise in intracellular Ca^{2+} in the DDAM region (Fig. 3d) showed that Ca^{2+} surged after a recognized delay¹⁰ (~50-100s) in response to flow (Fig. 3e, f). Yet, compared to the DDAM intensities, the Ca^{2+} signal did not show clear decreases during the flow-on time period, and Ca^{2+} intensity dropped slower than that of the DDAM after the flow-off time point.

The particular fluctuation of DDAM intensities in response to flow leads us to propose a new mechanism of mechanosensation in ciliated cells: a feedback sensor works as a negative modulator of DDAM polymerization and is activated automatically when DDAM reaches a certain density threshold. In this way, continued flow sensation prevents the DDAM from reaching polymerization saturation. To test this hypothesis, based on the fact that flow and Ca^{2+} rise are closely correlated in ciliated cells, we next used high-resolution confocal imaging to capture the dynamic responses of DDAM when we administered ionomycin³³ to increase cytosolic Ca^{2+} .

Surprisingly, mesh sizes of the DDAM demonstrated an obvious dynamic response: after initially becoming visibly denser, they gradually returned to pre-ionomycin levels (fig. 3g, h) within minutes. Our hypothesis is further supported by the observation that this dynamic feedback sensing process was dependent on the dose of ionomycin. When it was administered at a relatively high concentration, the ciliated cells responded acutely to a non-physiological Ca^{2+} increase: cilia disappeared and DDAM dissociated (Extended Data Fig. 4a, b) within ~5 mins. Cells sensitive to ionomycin also showed a mild form of this behavior following low dose administration: cilia were decapitated and DDAM fragmented (Extended Data Fig. 4c, d). In summary, DDAM responds to flow with a closed-loop dynamic process in which it adjusts its polymerization through a feedback modulator that depolymerizes when the mesh becomes dense and keeps cells in a sustainable homeostatic condition.

Ciliary trafficking is tuned by DDAM dynamics

To measure the effect of the flow induced DDAM polymerization and depolymerization on ciliary trafficking, we obtained time-lapse recordings of DDAM and ciliary trafficking vesicles after administration of low dose ionomycin (0.25uM, Fig.4a, Supplemental video 4). To extract outward transport of DDAM from passive motion segments, we segmented the trajectories of ciliary trafficking vesicles into directed motion (DM, orange) and anomalous diffusion (AD, blue) fragments (Fig. 4b, Methods). Time-lapse analysis of mean square displacement (MSD) plots of AD and DM showed a clear difference in their shapes: parabolic curves for DM, characteristic diffusion in a viscoelastic medium for AD (Fig. 4c). To calculate the ratio of DM κ in all trajectories, we built a DM-AD switch model to describe the distribution of instantaneous velocity of two fragments in all trajectories (Fig. 4d, Extended Data Fig. 5, supplemental materials).

Ionomycin first decreased the instantaneous velocity/diffusion coefficient for both DM and AD groups (Fig. 4e) and slightly reduced ciliary length. However, at the same time, the DM ratio increased significantly (Fig. 4f). The measured κ showed an apparent rise after DDAM polymerization triggered by ionomycin treatment. Before treatment, κ remained below 10 % ($7.56\% \pm 4.3\%$). After 0.25uM ionomycin treatment for 10 mins, the value of κ reached a peak of almost twice that of the baseline ($19.2\% \pm 7.3\%$). The distribution of instantaneous displacement $\Delta r(\tau)$ from DM segments showed that the increase came from those away from cilia (Fig. 2g, h), which are propelled by DDAM. All of the changes described above that were induced by ionomycin showed a trend toward a return to the pre-treatment level after ~20mins. We concluded that increased DDAM polymerization strengthens the centrifugal force. As a result, the fluid flow tuning the ciliary trafficking through DDAM also shows a dynamic process of feedback sensing.

Mechanical response of DDAM induced by flow

The time-lapse data in the previous section that we obtained for DDAM after ionomycin treatment also revealed a direct interaction between the actin fibers and the ciliary trafficking vesicles microscopically. We used the Line Filter Transform (LFT) and the Orientation Filter Transform (OFT) to augment the single filaments of the branched actin^{34, 35} that were blurred by the high turnover rate (Supplemental video 5). Here we show ciliary trafficking vesicles hitting and bending the actin fibers (Fig. 5 a), rebounding from the fibers (Fig. 5 b) or slowly zig-zagging in a trajectory influenced by the surrounding fibers (Fig. 5 c) over time. We found that the AD segments were composed of these trajectory parts of the direct interaction between vesicles and fibers. Also, MSD plots of the AD segments showed features of diffusion in viscoelastic medium (Fig. 4c). As a

result, we find that AD fragments are useful to measure the mechanical responses if vesicles are used as tracers and studied by the microrheology method³⁶.

The shape of the elastic modulus G' after 2 minutes changed from a slowly rising concave curve (red circles) to a rapidly rising convex curve (red triangles) with increasing frequency (Fig. 5d, Extended Data Fig. 6a). The first shape is commonly seen in measured cross-linked actin^{37,38}; the latter is reported as a unique feature of branched actin²⁶. Interestingly, the shape of the curve returned to concave at 15 mins. This resumption of the original shape agrees with our observation of DDAM depolymerization as the activation of the negative modulator. We used the non-muscle myosin II inhibitor, Y27632, to test whether the measured increased elastic modulus is caused by decreased mesh sizes. Administration of Y27632 increased the mesh sizes and reduced the elastic modulus (Fig. 5e-h). The increased mesh sizes of DDAM also reduced the centrifugal exclusion of the ciliary trafficking vesicles (Fig. 5l-m). The correlation between the mesh sizes and the elastic modulus was further confirmed by administration of a large dose of ionomycin. An acute and severe decrease in mesh size evoked a much more pronounced change in shape and amplitude in the mechanical response curves than the low-dose treatment (Extended Data Fig. 5b). Taken together, these results show that DDAM increases the mechanical responses when elevated intracellular Ca²⁺ increases its polymerization and that mesh sizes of DDAM can serve as a good indicator of the elastic modulus of DDAM.

PI(4,5)P₂ regulates depolymerization of DDAM

We hypothesized that a failure of DDAM dynamics could contribute to many flow-dependent diseases, including the increase in intraocular pressure in glaucoma. We tested this hypothesis in MEF cells obtained from a mouse model of congenital glaucoma (referred to as IOB mice) in which there is *Ocrl* gene knockout (details see Methods). Mutations in OCRL produce Lowe syndrome, a rare congenital condition characterized by ocular, renal and cerebral abnormalities³⁹. Surprisingly, we found that DDAM depolymerization was remarkably diminished in all IOB MEFs measured. The stagnation of actin turnover was clearly shown in a live-cell video recorded under the same imaging acquisition conditions as for wild type (WT) MEFs (Supplemental video 6). In Fig. 6a, three dashed lines show that the three long visible actin fibers persisted throughout the entire recording time of 6 mins. Ciliary trafficking vesicles appeared to swing along the fibers instead of proceeding by a zig-zag movement (Fig. 6b). In the distance-time graph of the trajectories, the traces of single vesicles showed “S” shapes rather than the collective skewed slopes of control cells (Fig. 6c). The G' measured from the AD segments showed that the elastic modulus of the IOB MEFs was much lower than in control cells (Fig. 6d). After ionomycin treatment, IOB MEFs showed more rapid condensation of DDAM structure (Fig. 6e) and increased G' (Fig. 6f) than control cells due to decreased actin depolymerization.

Actin accumulation in response to flow was evident in more than half of the cells that we recorded (Fig. 6g, i, j). The DDAM fluorescence intensities showed a plateau instead of a decrease as in WT MEFs after the flow was ceased. We also found that the IOB MEFs were more susceptible to flow stimulation than control cells. We observed cells shrink, shed cilia (images not shown), and in some cases, form unstable cilia with an abnormal “Y” shape during flow stimulation (Fig. 6h,

Supplemental video 6). OCRL controls the dephosphorylation of PI(4,5)P₂ on the plasma membrane³⁹. We confirmed that PI(4,5)P₂ accumulated near the cilia in MEFs, whereas it was depleted in WT cells (Fig. 6k-l). Therefore, we concluded that PI(4,5)P₂ controls DDAM depolymerization.

Gelsolin as a feedback sensor of the DDAM mechanosensation loop

Gelsolin is a potent actin severing protein⁴⁰ that is regulated by both PI(4,5)P₂ and calcium^{41, 42}. A gene screen study also reported that it is a mechanical checkpoint³ that modulates cell proliferation³. Next, to rescue the DDAM depolymerization in IOB MEFs that we described in the previous section, we introduced GelsolinN^{43, 44}, a constitutively active form of gelsolin that continues its severing activity regardless of intracellular Ca²⁺ concentration, to compensate for the inhibition of gelsolin by PI(4,5)P₂. As a result, we observed that DDAM accelerated single fiber turnover with a corresponding decrease in the actin mesh sizes (Fig. 7a). We previously reported that certain molecules (e.g., SMO) are not transported to primary cilia in Ocrl -deficient MEF cells⁴⁵. Surprisingly, GelsolinN restored not only the transportation of SMO to cilia but also the region devoid of vesicles, which is not normally observed in IOB MEFs (Fig. 7b, Supplemental video 7). The distance-time graph indicates that the collective right-skewed slopes have been restored (Fig. 7c). Aligned with the decreased size of the mesh, the elastic modulus measured from trajectories of SMO also increased (Fig. 7d). Taken together, we conclude that gelsolin serves as one of the negative modulators in the closed-loop dynamics of mechanosensation in ciliated cells.

Discussion

A closed-loop model of mechanosensation in ciliated cells

In this study, we characterized the dual “motor” and “sensor” functions of an actin structure (DDAM) newly discovered in ciliated cells that enables a closed-loop control of ciliary trafficking, which ultimately couples external flow signals and ciliary signaling. Negative feedback modulators such as gelsolin ensure that an increase in the mechanical response of the DDAM automatically evokes its depolymerization. This dynamic process continuously keeps ciliated cells responding rapidly and interprets the flow so as to sustain homeostasis (Fig. 7e). The classic GPCR style of mechanosensation model that is based on activation of ion-channels/receptors generates a flow response curve like that of Ca^{2+} (Fig. 4e), which is not affected by its downstream signaling. In contrast, the closed-loop model avoids system breakdown by reducing actin condensation over time and produces sustainable control of flow-sensing in a complex extracellular environment.

This model fits well with the experimental results that we obtained in the three different cases (Fig. 7f). In quiescent IOB MEFs, Ocrl knockout causes accumulation of PI(4,5)P₂ in the plasma membrane, which inhibits actin severing by gelsolin. In static culture medium, stagnant depolymerization traps ciliary vesicles in the actin fibers that persist for a long time and causes less ciliogenesis and shorter cilia⁴⁶. When flow is activated, failure of negative modulation quickly saturates the mechanical limit of the actin network, causing cilia to be shed or to become unstable. In normal healthy cells, PI(4,5)P₂ content is low around cilia, and the actions of ciliary trafficking, gelsolin, Ca^{2+} , and external force are in homeostasis. When flow occurs, DDAM responds immediately by polymerizing and increasing the elastic modulus to balance flow pressure. At the onset of the subsequent period of Ca^{2+} rise and gelsolin activation, polymerization of the DDAM

peaks before gelsolins initiate depolymerization. After several cycles, polymerization and depolymerization produce a new equilibrium of ciliary trafficking, gelsolin, Ca^{2+} and flow pressure. Our model reveals new pathways for the pathogenesis of flow-dependent disorders such as glaucoma and polycystic kidney disease and provides possible explanations why diseased cells react badly to flow and lose their cilia. Our model also starts to elucidate the role of primary cilia in many fundamental proliferation and differentiation pathways controlled by mechanical force.

DDAM as readout of cellular mechanical responses

The discovery of the DDAM as a critical component in the rapid dynamic response to fluid flow provides a new readout for studying mechanical responses of live cells. Compared to the standard current methods, such as force microscopy or localization of transcriptional factors like YAP/TAZ, changes in the mesh sizes (Fig. 5) or general fluorescence intensity of DDAM (Fig. 3) provide an accurate readout in minutes of cellular mechanical responses that can be identified with common microscope settings. This readout will be extremely useful in studying the various types of mechanical stimulation associated with Ca^{2+} rise in the cytosol of ciliated cells, including flow, direct cell-cell contact⁴⁷ and stretching of the cells in tissue².

Cilium frequency and length have been reported to be correlated with the intracellular localization of YAP/TAZ²⁴. Indeed, because ciliary trafficking is tuned by extracellular force, the length and frequency of primary cilia to a certain degree reflect cellular mechanical responses. However, our study shows that this indicator is less accurate than DDAM mesh size. For example, primary cilia are shortened both when the elastic modulus is low due to stagnant depolymerization in IOB MEFs and when the elastic modulus is high due to excision of cilia.

Figures and legends:

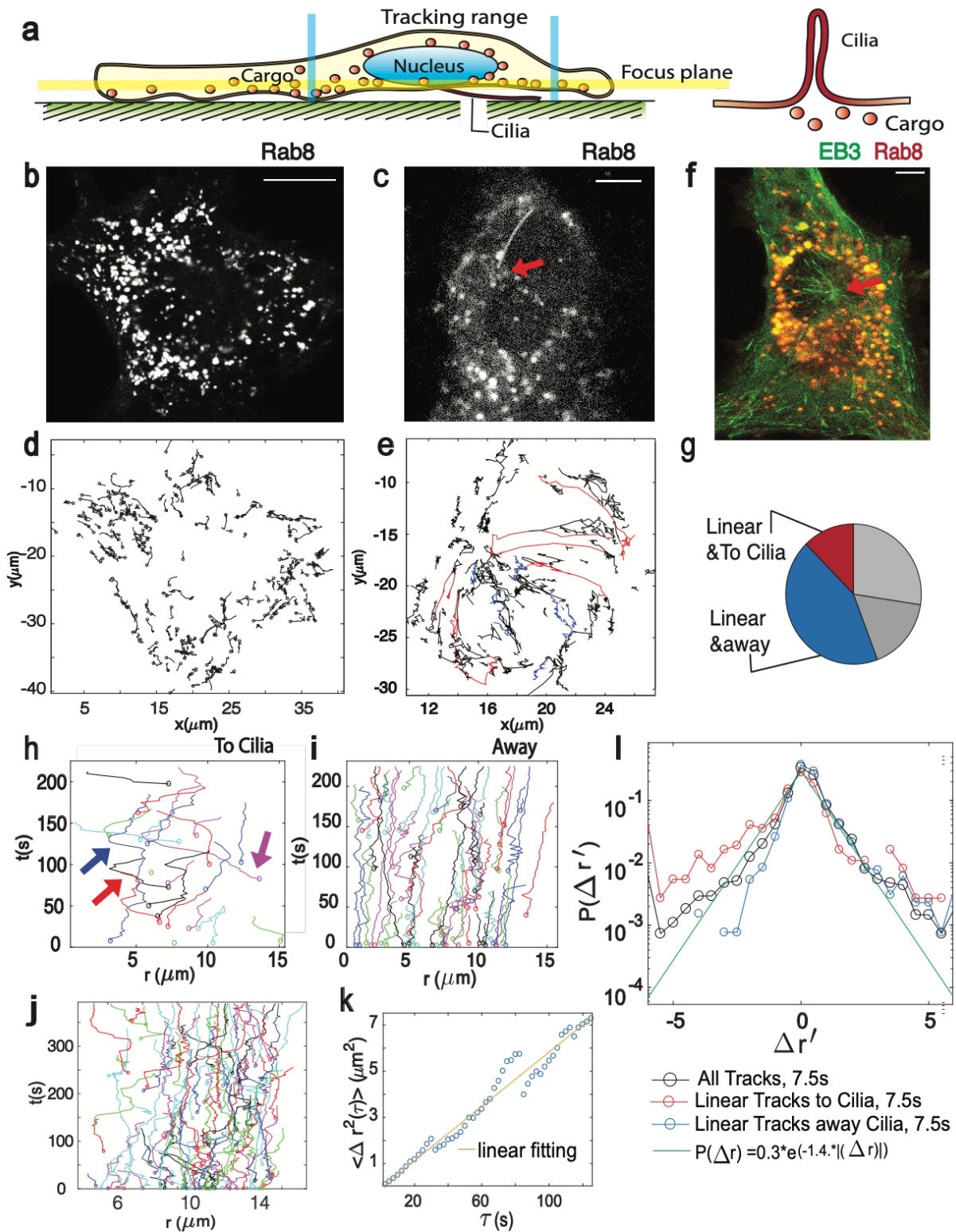
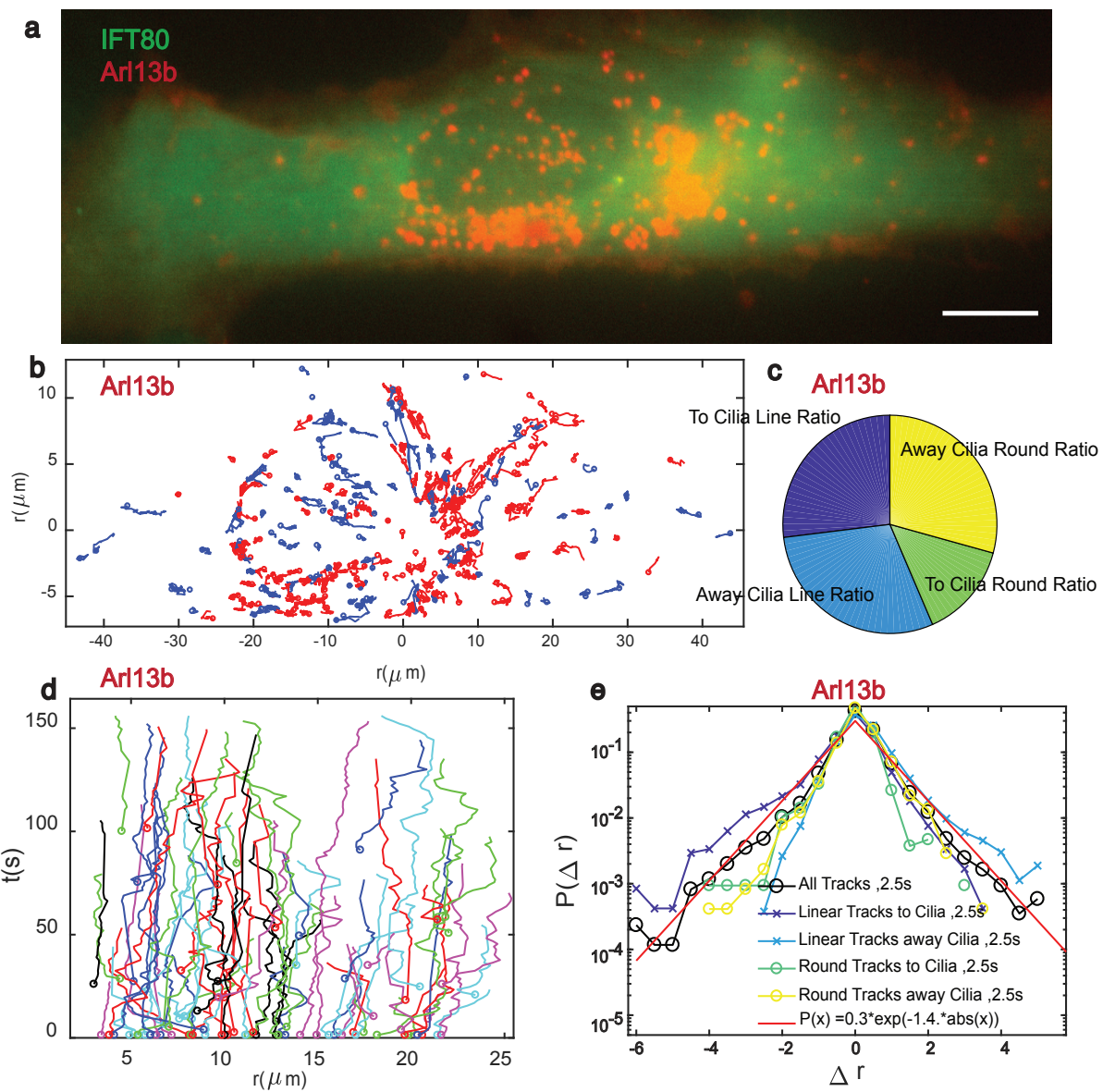


Fig. 1. Exclusion of ciliary targeting vesicles revealed by single vesicle tracking of Rab8

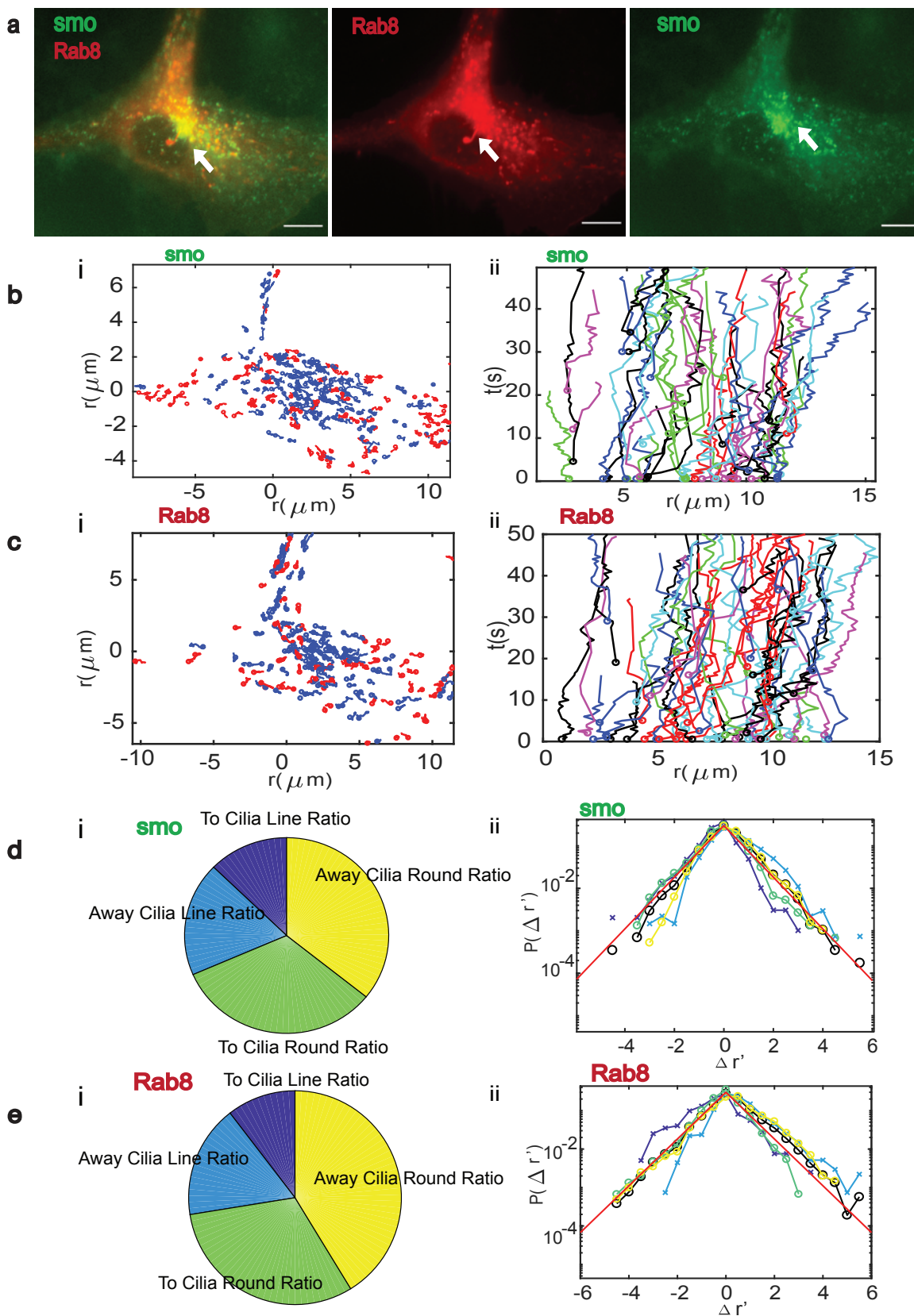
- a.** Cartoon illustrations of the experimental setup to record cargo vesicles. Left: Sectional view to show the focus plane selection for recording the motion of vesicles at the base of the cilia. Right: Sectional view of the cilia and cargo vesicles labeled by Rab8, SMO or Arl13b. By this method cilia and cargo vesicles can be labeled simultaneously in a single color.
- b.** Representative image of a MEF expressing Rab8-mCherry that labels intracellular vesicles in a non-ciliated cell. Scale bar is 10 μm ($n = 10$ cells, 3 independent experiments).
- c.** Trajectories of Rab8-labeled vesicles obtained from the same cell in **b** from a video 4 min long recorded at 1.3 s per frame.
- d.** Representative image of an hRPE1 cell expressing Rab8-mCherry that labels cargo vesicles and cilia (base of cilia, red arrow). Scale bar is 5 μm . Supplemental video 1 shows vesicle motions in the focus plane at the cilia base in the same cell ($n = 36$ cells, 8 independent experiments).
- e.** Trajectories of ciliary trafficking cargo vesicles obtained from the same cell as in **c** from a video 4 min long recorded at 2.5 s per frame for Rab8-mCherry labeled vesicles. Red lines show the 5 linear tracks going to the cilia and blue lines show 5 linear tracks going away from the cilia.
- f.** Representative image of an hRPE1 cell expressing Rab8-mCherry, which labels cargo vesicles and cilia, and EB3-GFP, which labels microtubules (base of cilia, red arrow). Scale bar is 5 μm . also see supplemental video 1.
- g.** The distance-time graphs for trajectories going backward from the cilium with slow zig zags away from the cilium.
- h.** The distance-time graphs of the distance r between the vesicle and cilium along with time t for trajectories in a non-ciliated MEF.
- i.** The distance-time graphs for forward trajectories to the cilium, with large advancement to the cilia and slow zig zags away from the cilia. Arrows point to the three large displacement segments in three different trajectories of the corresponding color.
- j.** Plots of the ratio of forward linear trajectories (red), backward linear trajectories (blue) and non-linear trajectories (grey).
- k.** Measured mean square displacement (MSD, blue circles) from all the trajectories in **e**. Linear fitting (yellow) in time τ of 0~150s generates the diffusion coefficient $D_L = 0.015 \mu\text{m}^2/\text{s}$.
- l.** PDF plot of instantaneous distance to the cilia base ($\Delta r'$) during the time τ of 7.5s for linear trajectories (circles, black lines), forward linear paths (stars, red line), and backward paths (stars, blue line). The black fitting line is $P(\Delta r') = 0.3.* e^{(-1.4|\Delta r'|)}$.



Extend Data Fig.1 Out transport of ciliary targeting vesicles revealed by single vesicle tracking of Arl13b. This figure relates to Fig. 1.

- a.** Representative image of an hRPE1 cell steadily expressing IFT80-GFP that labels cilia, and transiently expressing Arl13b-mCherry that labels cargo vesicles and cilia. The white arrow points to the base of the cilia. Scale bar is 5 μm . Supplemental video 1 shows the vesicle motions in the same cell ($n = 9$ cells, 3 independent experiments).
- b.** Trajectories of ciliary trafficking cargo vesicles obtained from the same cell as in (a); from a 1 min video of Arl13b-mCherry labeled vesicles recorded at 0.5 s per frame. Each trajectory has a circle at the beginning to label the start location. Red lines show tracks going toward the cilia and blue lines show tracks going away from the cilia.

- c.** Plots of the ratio of forward linear trajectories (purple), backward linear trajectories (blue), forward round trajectories (green), and backward round trajectories (yellow).
- d.** The distance-time graph of the distance \mathbf{r} between vesicles and cilia along with time \mathbf{t} for all trajectories. Most trajectories feature a slowing zig zag away from cilia; a few large displacements toward cilia. The trajectory data are the same as from **b**.
- e.** PDF plot of instantaneous distance to the cilia base ($\Delta r'$) during the time τ of 1.5s for all trajectories (circles, black lines): forward linear (stars, purple line), backward linear (stars, blue line), forward round (circles, green line), and backward round (circles, yellow line). The black fitting line is $P(\Delta r') = 0.3 \cdot e^{(-1.4|\Delta r'|)}$. The trajectories data are the same as from **b**.



Extend Data Fig.2. Out transport of ciliary targeting vesicles revealed by single vesicle tracking of smoothened (SMO) and Rab8. This figure relates to Fig. 1.

- a.** Representative image of an hRPE1 cell transiently expressing Rab8-mCherry and YFP-SMO that label cargo vesicles and cilia. The white arrows point to the base of the cilia. Scale bar is 5 μ m. Supplemental video 1 shows the vesicle motions in the same cell. ($n = 10$ cells, 4 independent experiments).
- b.** Single vesicle tracking analysis for YFP-SMO. i. Trajectories of ciliary trafficking cargo vesicles obtained from the same cell as in **(a)**; from a 1 min video of YFP-SMO labeled vesicles recorded at 0.5 s per frame. Each trajectory has a circle at the beginning to label the start location. Red lines show tracks going toward cilia and blue lines show tracks going away from cilia. ii. The distance-time graph of the distance r between vesicle and cilia along with time t for all trajectories. Most trajectories feature a slowing zig zag away from cilia; a few large displacements toward cilia. The trajectory data are the same as from **(b)**.
- c.** Single vesicle tracking analysis for Rab8-mCherry. Same plots of i, ii, iii as for **b**.
- d.** i. PDF plot of instantaneous distance to the cilia base ($\Delta r'$) during the time τ of 1.5s for all trajectories (circles, black lines): forward linear (stars, purple line), backward linear (stars, blue line), forward round (circles, green line), and backward round (circles, yellow line). The black fitting line is $P(\Delta r') = 0.3 \cdot e^{(-1.4|\Delta r'|)}$. The trajectories data are the same as from **(b)**. ii. Plots of the ratio of forward linear trajectories (purple), backward linear trajectories (blue), forward round trajectories (green), and backward round trajectories (yellow) for SMO (left) and Rab8 (right).
- e.** Single vesicle tracking analysis for Rab8-mCherry. Same plots of i, ii as for **d**.

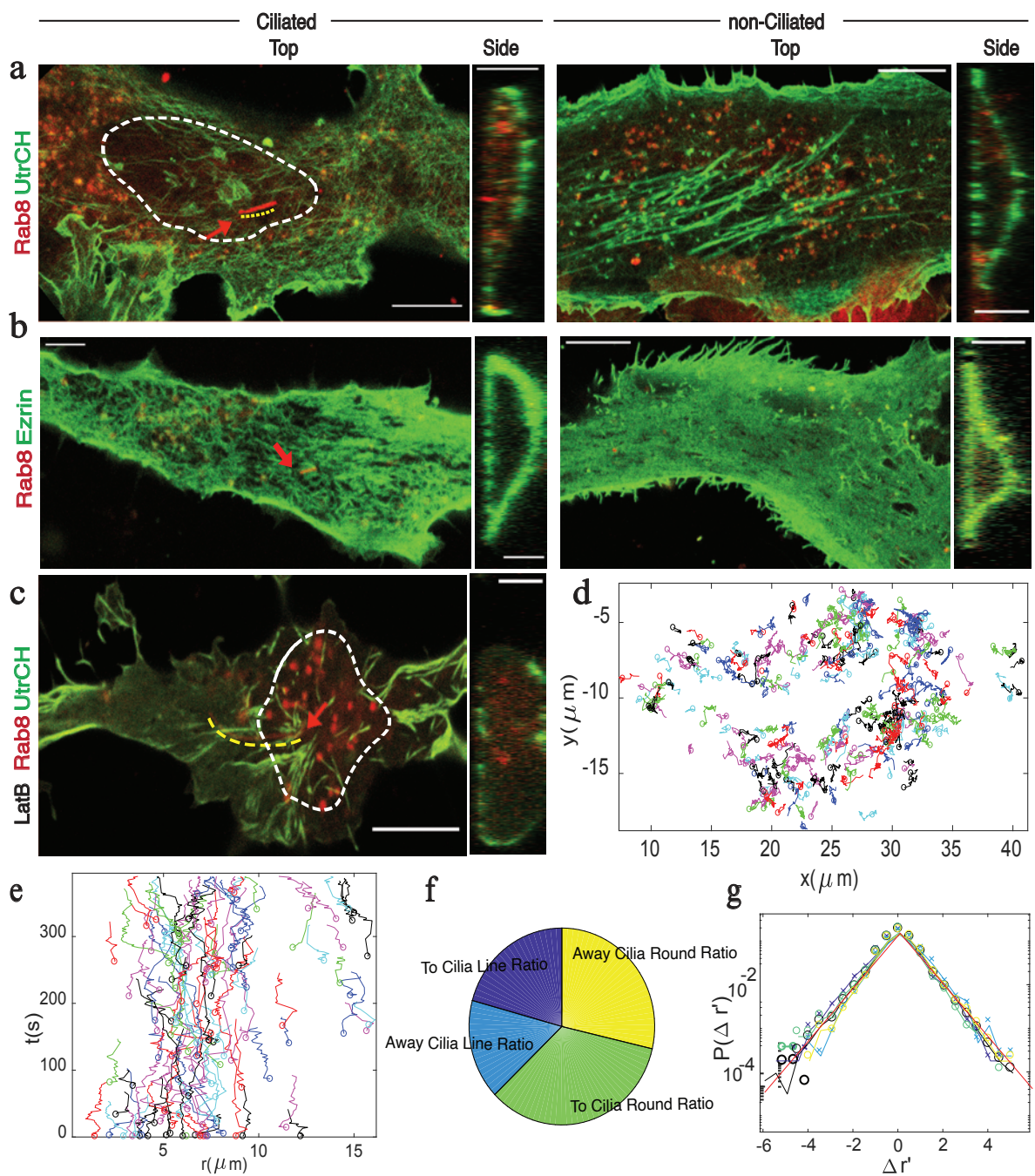


Fig. 2. Highly dynamic branched actin networks generate the centrifugal force.

a. Representative image of an hRPE1 cell transiently expressing Rab8-mCherry and UtrCH-EGFP. Ciliated, left: a single slice image focused on a plane ~ 400-600nm from the bottom of the cell and 400nm in thickness. Rab8-labeled vesicles and the branched actin networks in this focus plane are at the same height as the ciliary base. The red arrow points to the base of the cilia. White dash lines show the vesicle clear region, yellow dash line shows the cilia. Scale bar is 10 μ m. Supplemental video 2 shows the same cell. Right: side view, showing depleted actin

around the cilia. Scale bar is 5 μm ($n = 20$ cells, 8 independent experiments). Non-ciliated, left: a single slice image obtained from a similar location as in the ciliated cell for a non-ciliated control hRPE1 cell transiently expressing Rab8-mCherry and UtrCH-EGFP. The single actin fiber is thickened and less dynamic around the nuclear region. Right: side view showing actin evenly distributed around the cell. Scale bar is 5 μm ($n = 9$ cells, 3 independent experiments). Code system for red arrows and scale bars applies to **b** and **c**.

b. Representative image of an hRPE1 cell transiently expressing Rab8-mCherry and Ezrin-GFP. Ciliated, left: a single slice image obtained at a similar location as in **a(i)**. Right: side view showing depleted ezrin around the cilia ($n = 15$ cells, 4 independent experiments). Non-ciliated, left: a single slice image obtained from a similar location as in the ciliated cell for a non-ciliated control hRPE1 cell transiently expressing Rab8-mCherry and Ezrin-EGFP. Right: side view showing ezrin evenly distributed around the cell ($n = 10$ cells, 3 independent experiments). Also see Supplemental video 2.

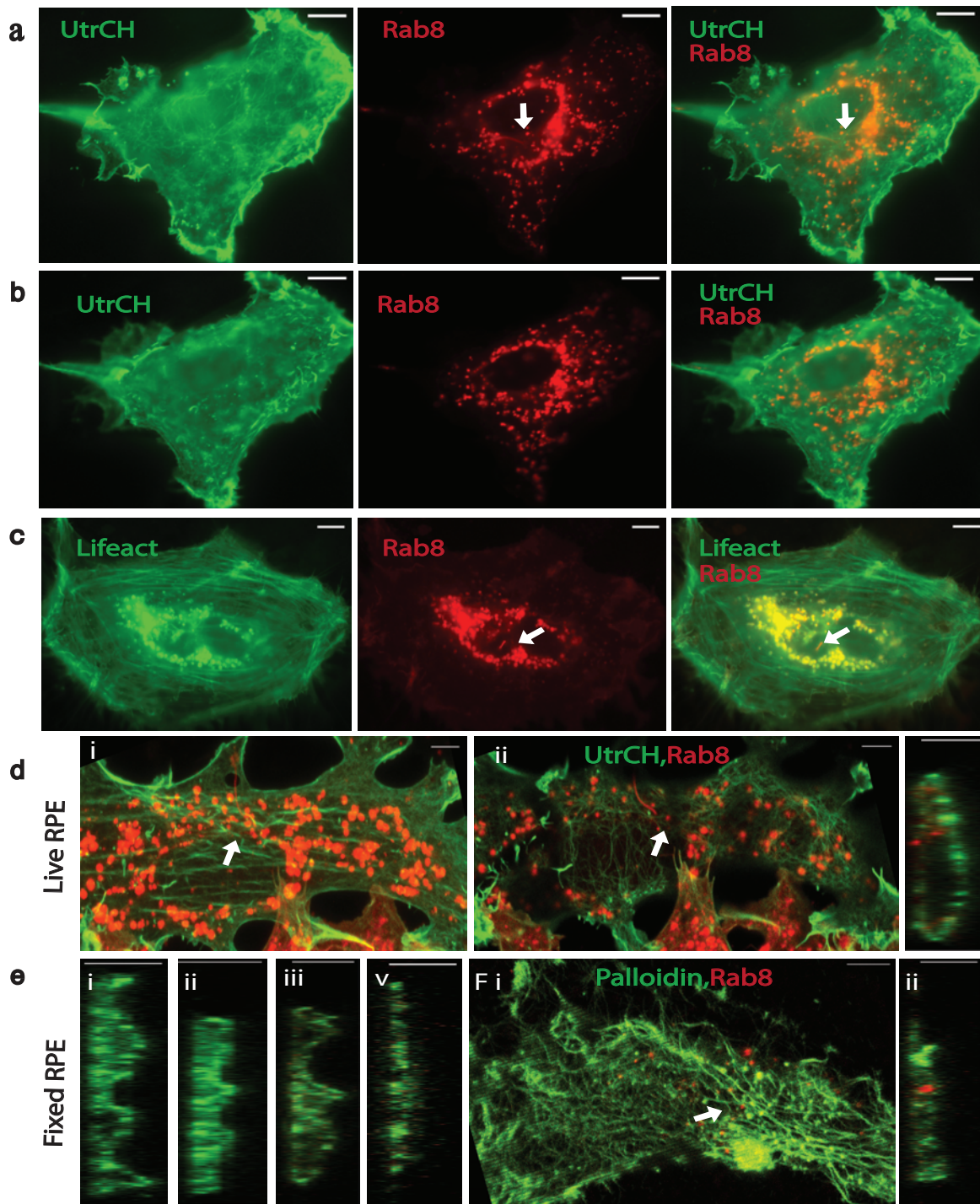
c. Representative image of an hRPE1 cell transiently expressing Rab8-mCherry and UtrCH-EGFP after treatment with latrunculin B (LatB). White dash lines show the vesicle clear region, yellow dash line shows the cilia. Scale bar is 10 μm . Left: a single slice image obtained at a similar location as in **a**. Vesicles labeled by Rab8 crowd around the ciliary base. Right: side view showing depleted branched actin throughout the cell ($n = 12$ cells, 4 independent experiments).

d. Trajectories of ciliary trafficking cargo vesicles labeled for Rab8-mCherry obtained from the same cell as in **c**; from a 6 min video recorded at 1.3 s per frame. Each trajectory has a circle at the beginning to label start location.

e. The distance time graph for all trajectories in **d**. Most trajectories lose the feature of a slowing zig zag away from cilia, as in untreated cells, and become more random.

f. Plots of the ratio of forward linear trajectories (purple), backward linear trajectories (blue), forward round trajectories (green), and backward round trajectories (yellow). Trajectory data are the same as from **d**.

g. PDF plot of instantaneous distance to the cilia base ($\Delta r'$) during the time τ of 1.5s for all trajectories (circles, black lines): forward linear (stars, purple line), backward linear (stars, blue line), forward round (circles, green line), and backward round (circles, yellow line). The black fitting line is $P(\Delta r') = 0.3 \cdot e^{(-1.4|\Delta r'|)}$. Trajectory data are the same as from **d**.



Extend Data Fig.3. Location of the DDAM and comparison of actin labeling methods. This figure relates to Fig. 2.

a. Representative image of an hRPE1 cell transiently expressing Rab8-mCherry and UtrCH-EGFP. In the GFP channel, an actin web structure spreads out around the nuclear region; in the

mCherry channel, Rab8 labeled vesicles and cilia. White arrow points to the base of the cilia, where branched actin networks create a region clear of vesicles. Supplemental video 2 shows the motion and dynamic interaction of vesicles and actin fibers in this cell ($n = 8$ cells, 3 independent experiments).

b. The same cell with the focus plane moved up $1\mu\text{M}$ in the z direction. In the GFP channel, the branched actin web is not visible; in the Rab8 channel, the cilia are not visible.

c. Representative image of an hRPE1 cell transiently expressing Rab8-mCherry and Lifeact-EGFP. The focus is on the base of the cilia. In the GFP channel, actin fibers organize stress fiber-like structures with a turnover much lower than that of the DDAM. In the mCherry channel, the cilia, vesicles, and vesicle-clear region around the ciliary base indicated by the white arrow still remain. Supplemental video 2 shows the motion and dynamic interaction of vesicles and actin fibers in this cell ($n = 20$ cells, 3 independent experiments).

d. (i) Maximum intensity projection (MIP) of an hRPE1 cell transiently expressing UtrCH-GFP and Rab8-mCherry. The branched actin web is not visible. (ii) Left: an image slice obtained under the same conditions as in fig 2a. The cilia and branched actin networks are much more apparent. Right: side view from the z-stack images of the same cell as in the left image; the actin is obviously depleted around the cilia. This figure is from the same data set as in Fig. 2a and shows how the MIP image hides the DDAM.

e. Representative side view image of four hRPE1 cells transiently expressing Rab8-mCherry and stained with phalloidin 488 after fixation. Side views of fixed cells show that the top and bottom cortex collapse together, in stark contrast to the side views of live cells.

f. (ii) Left: an image slice obtained under the same conditions as in fig 2A from an hRPE1 cell transiently expressing Rab8-mCherry and stained with phalloidin 488 after fixation. Branched actin networks blend in with actin web fibers and do not show distinguishing features. Right: side view from the z-stack images of the same cell as in the left image showing actin from top and bottom planes collapsed together.

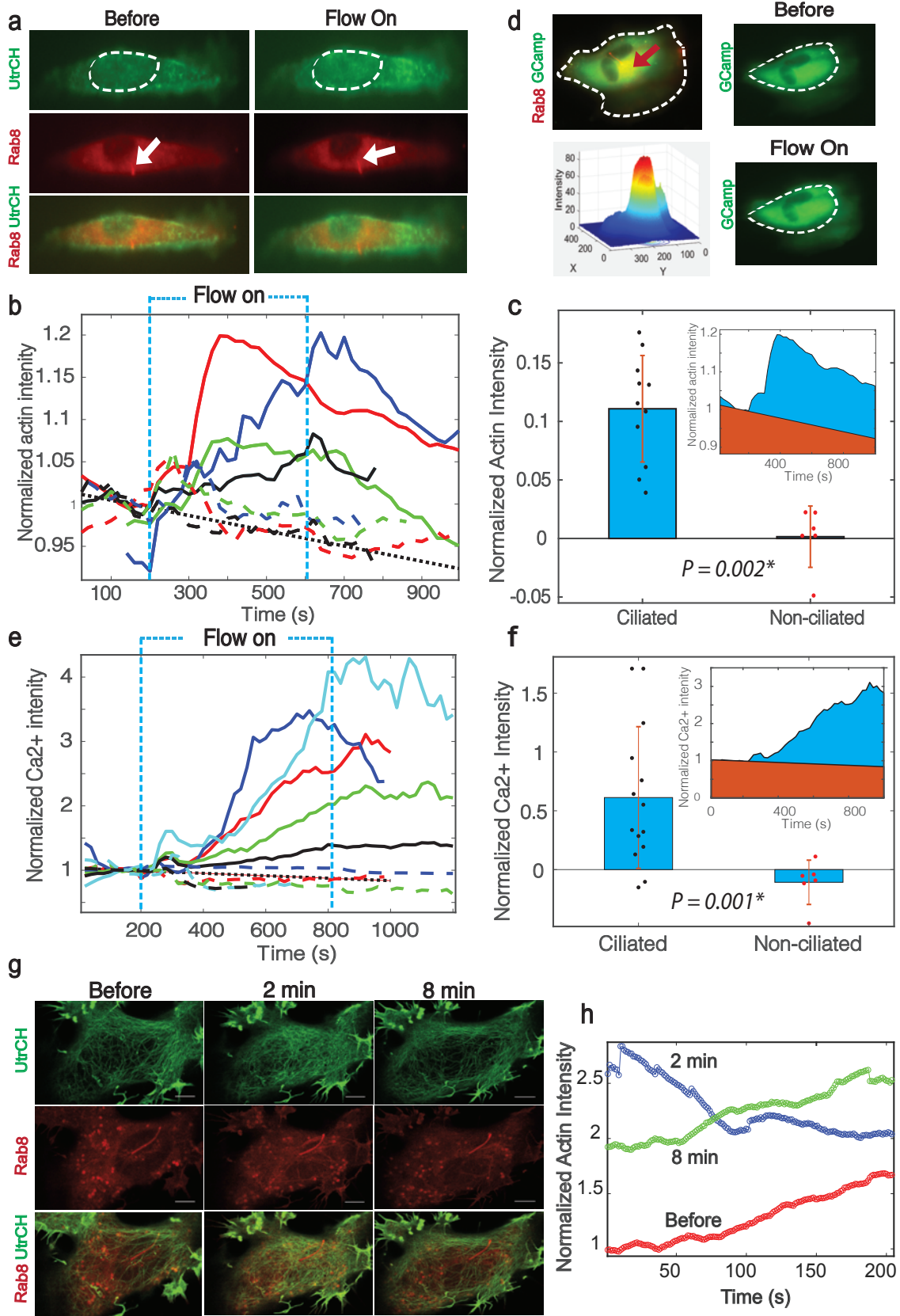
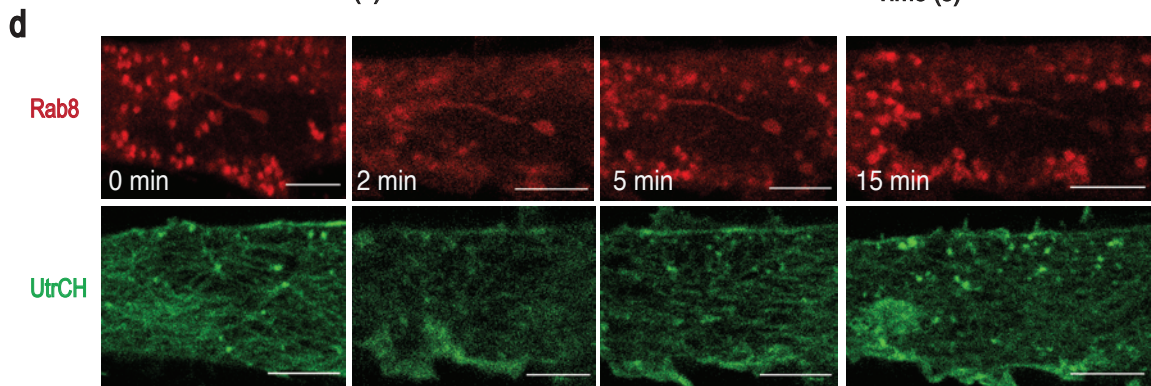
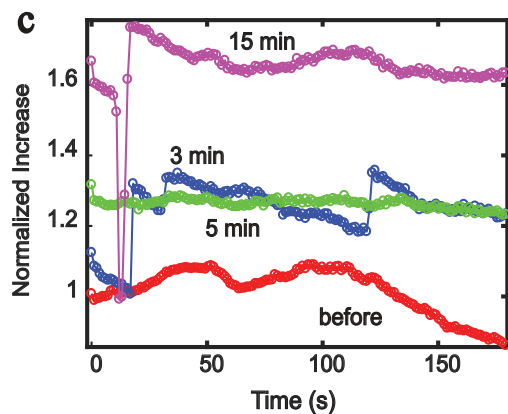
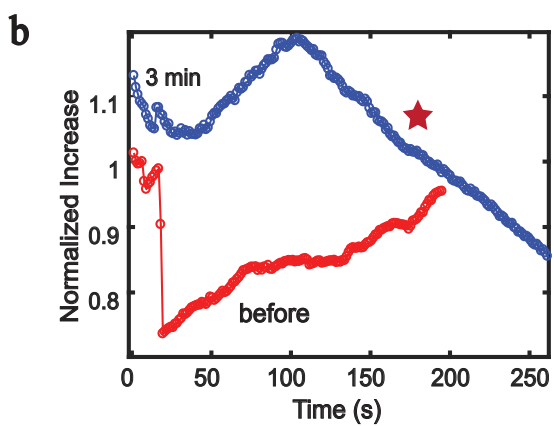
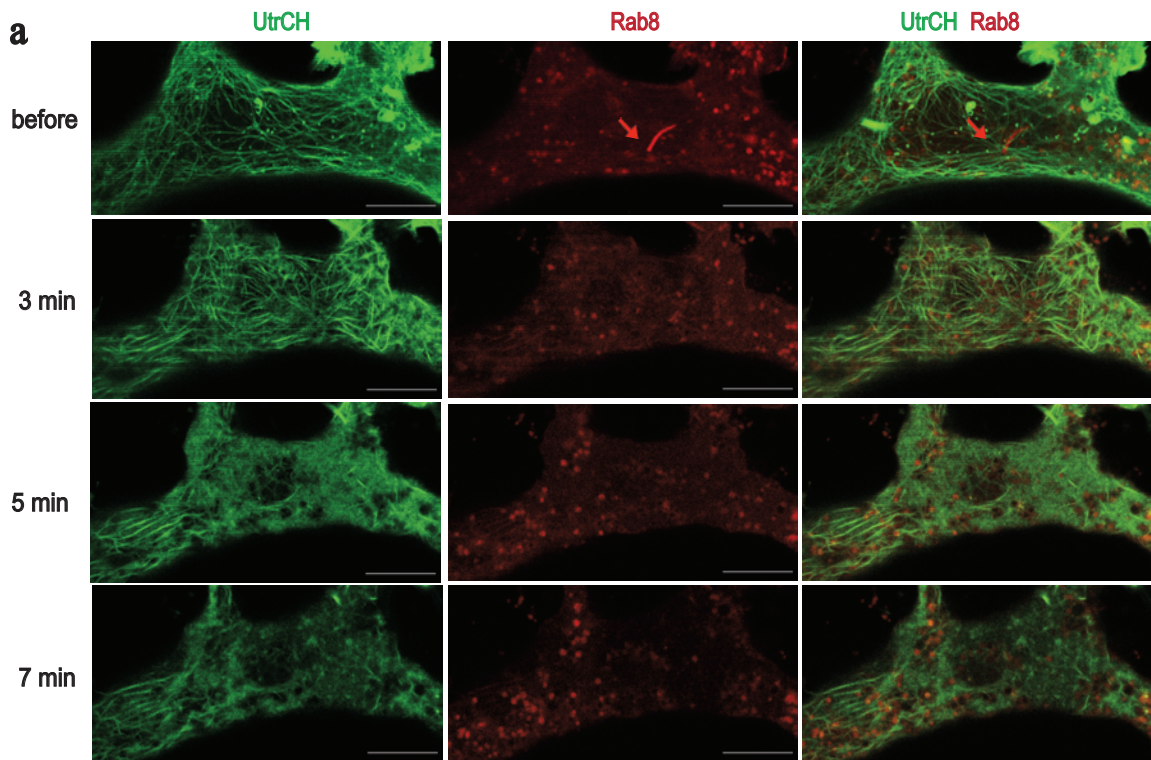


Fig. 3 Dynamics responses of DDAM to mechanical and calcium signals demonstrate feedback sensing

- a.** Representative image of an hRPE1 cell transiently expressing Rab8-mCherry and UtrCH-GFP before and after flow is applied for 5 min. White arrows show the location of the ciliary base. See also supplemental video 3.
- b.** Normalized branched actin intensity in response to flow. Normalized fluorescence intensity of ciliated cells (solid lines) and non-ciliated cells (dashed lines). The black dotted line shows a base reference line of the photobleaching caused by imaging. Blue dashed line block shows the time period when flow is on.
- c.** Statistics of the area covered in the flow chart, as shown in **b** for ciliated cells and non-ciliated cells. The area covered by the reference photobleach line (indicated in orange) has been subtracted from the measured individual areas. Dots on the bar plot show the measured value of the individual areas ($n = 16$ cells, $p = 0.002$, 5 independent experiments).
- d.** Representative image of an hRPE1 cell transiently expressing Rab8-mCherry and the GCamp6f before and after flow is applied. The white dashed line in the dual colored image encircles the area of the cell. The red arrow points to the cilia base. The white dashed line in the single colored images shows the area of DDAM. Pseudo-color plot of calcium signal after 3 min of flow stimulation. The calcium signal rises far higher in the center than in other regions of the cell. The time-lapse data is recorded from the same cell as in **b**. See also supplemental video 3.
- e.** Normalized calcium intensity in response to flow. Same color code as in **b**.
- f.** Statistics of the area covered in the flow chart shown in **e** for ciliated and non-ciliated cells. Same color code as in **c** ($n = 13$ cells, 4 independent experiments).
- g.** Time-lapse images of the same cell before and after treatment with $0.25\mu M$ ionomycin for 2 min and 8 min. The branched actin networks become denser and then again become sparse; cilia are preserved through the whole process. See also supplemental video 3.
- h.** Branched actin polymerization in response to ionomycin. Normalized actin intensity is calculated for three 5 min videorecordings of a ciliated hRPE1 cell before (red) and after $0.25\mu M$ ionomycin treatment for 2 min (blue) and 8 min. In order to compare the response over time, the single channel actin intensity is normalized by the fluorescence intensity of DDAM measured at 10th frame of the video of before-treatment ($n = 10$ cells, 5 independent experiments).



Extend Data Fig.4. Response of the branched actin networks to different concentrations of ionomycin. This figure is related to Figure 3.

- a. Time-lapse images of a ciliated hRPE1 cell before and after 2.5 μ M ionomycin treatment for 2 min, 5 min, and 8 min. The branched actin networks acutely become denser with much thicker individual fibers, then quickly dissolve within 7 min. Red arrow points to the base of the cilia. Cilia are shed within 3 min of adding ionomycin. Also see supplemental video 4 (n = 9 cells, 5 independent experiments).
- b. Plot of the normalized increase of branched actin in response to 2.5 μ M ionomycin. Normalized increase is calculated in the same fashion as in Fig. 3(f) from two 300s video-recordings for a ciliated hRPE1 cell before (red) and after 0.25 μ M ionomycin treatment. The star labels the steady decrease of the actin signal resulting from dissolution of the actin network, as shown in (a).
- c. Branched actin polymerization in response to 0.25 μ M ionomycin treatment. Normalized increase is calculated as in Fig.3(f) from four 200s video-recordings of a ciliated hRPE1 cell before (red) and after ionomycin treatment for 3 min (blue), 5 min (green), and 15 min (magenta) (n = 10 cells, 5 independent experiments, same data set as Fig 3g).
- d. Time-lapse images of a ciliated hRPE1 cell before and after 0.25 μ M ionomycin treatment for 2 min, 3 min, 5 min, and 15 min. The actin increase is less obvious than with the high concentration treatment shown in Extend Data Fig 4 (a, b). This recording also shows an example of ciliary tip excision, but most of the cilia are preserved over the time of the recording. White arrows point to the base of the cilia.

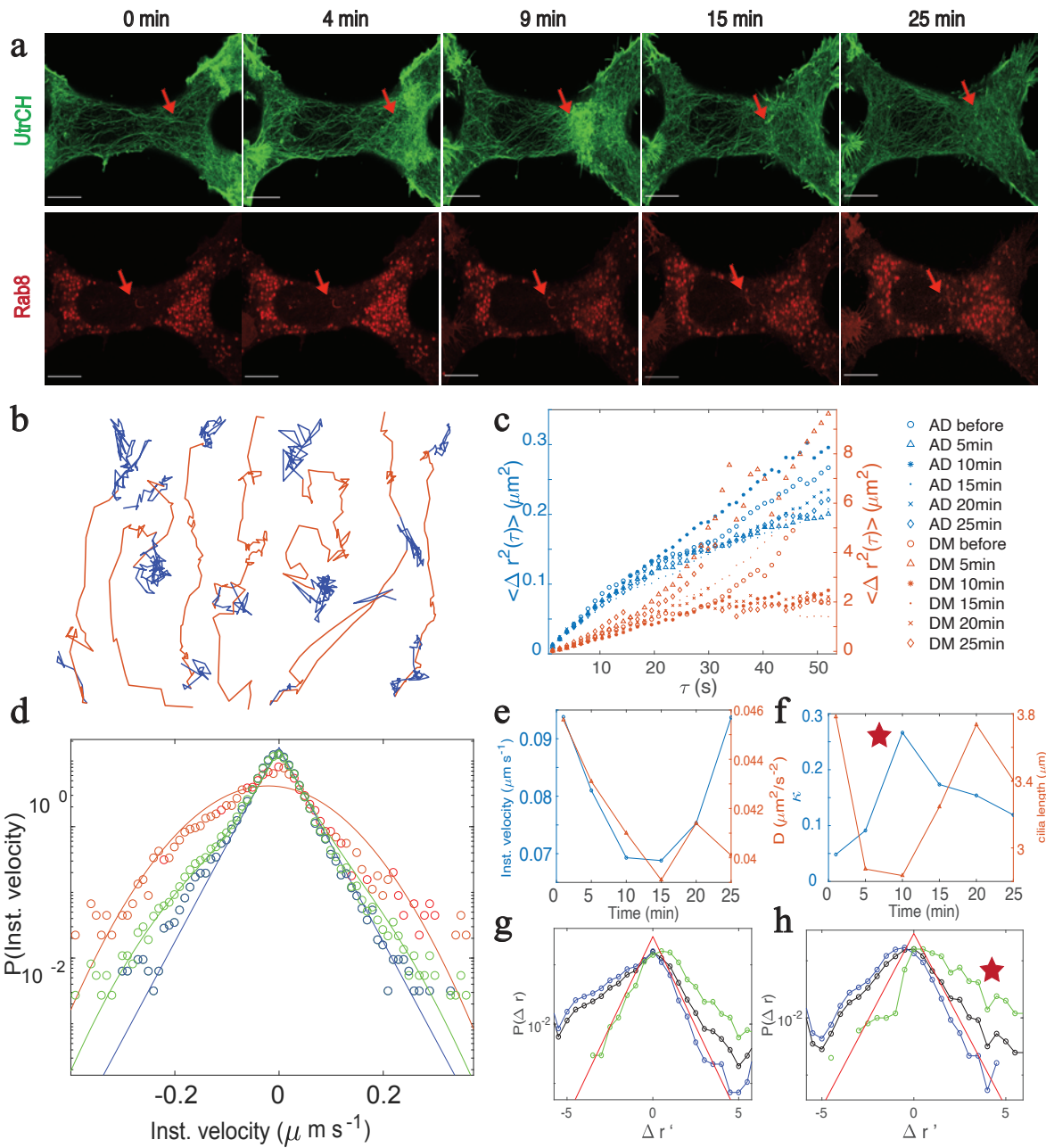


Figure 4 Ciliary trafficking is turned by DDAM dynamics

a. Time-lapse images of a ciliated hRPE1 cell transiently expressing Rab8-mCherry and UtrCH-GFP before and after 0.25 μ M ionomycin treatment for 5 min, 10 min, 15 min and 25 min. The GFP channel shows that actin processes condense around the cilia and later gradually resume a structure similar to that before treatment. Red arrows point to the most obvious actin change. The mCherry channel shows that cilia are preserved at all times during the recording; red arrows point to the base of the cilia ($n = 10$ cells, 5 independent experiments). See also supplemental video 4.

b. Representative linear trajectories that have been segmented for directed motion (DM, orange) and anomalous diffusion (AD, blue) trajectories. Individual vesicles commonly switch between the two motions over time.

c. Plot of the mean square displacement (MSD) of DM (orange) and AD (blue) trajectories obtained from three min-long videos beginning before or 4, 9, 15, 20, and 25 min after administration of 0.25 μ M ionomycin. The MSD plots of DM trajectories are parabolic and their $\langle \Delta r^2(\tau) \rangle$ in the same region of the lag time τ is higher than the AD ones. The MSD of the AD trajectories features three linear segments as diffusion in a viscoelastic medium.

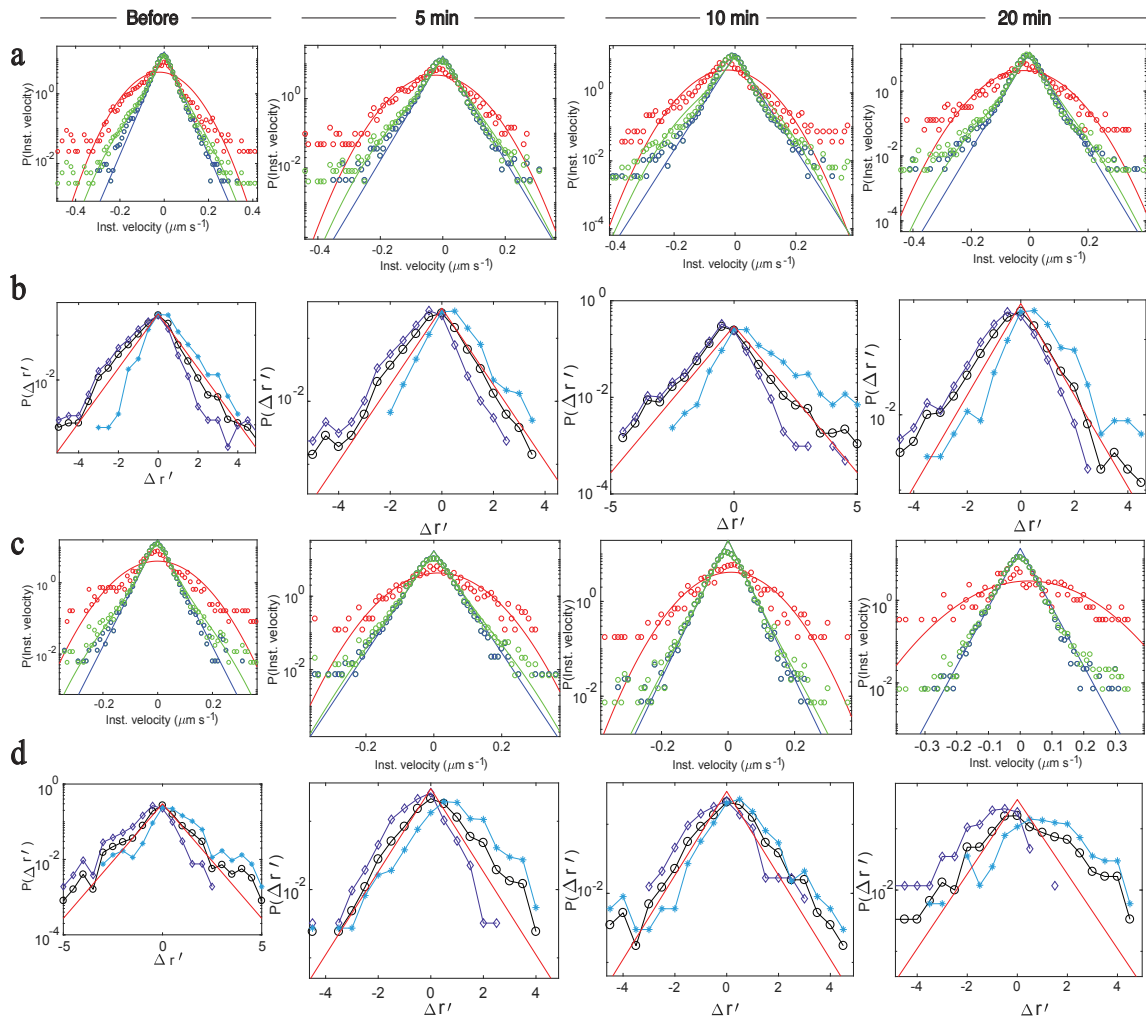
d. Plots of the probability density function (PDF) for instantaneous velocity of the DM trajectories (red circles), AD trajectories (blue circles), and all trajectories (green circles) obtained from three min-long videos recorded before ionomycin treatment. PDF plots for instantaneous velocity of trajectories at other time periods are shown in Figure 4s. The red line shows the result of fitting the Gaussian function to the PDF of DM trajectories; the blue line shows the result of fitting the exponential curve to the PDF of AD trajectories; the green line shows the result of fitting the DM and AD switch model to all trajectories.

e. Plot of the change of the directed motion ratio κ in all trajectories, and the ciliary length measured from the beginning frame of each recording. The star shows a clear rise in directed motion ratio after treatment with ionomycin.

f. Plot of the change of the diffusion coefficients for the AD trajectories (blue), and the instant velocity of the DM trajectories (orange) before and 4, 9, 15, 20, and 25 min after 0.25 μ M ionomycin treatment. The diffusion coefficients are obtained from linear fitting to the first 6 points of their MSD plots; the instant velocities are obtained from parabolic fitting to the first 30 points of their MSD plots. Both quantifications of trafficking speed show a clear decrease in diffusion coefficients/ instant velocities after ionomycin treatment, followed by recovery.

g. PDF Plots $P(\Delta r')$ for normalized instantaneous displacement $\Delta r'$ during the time lag $\tau = 6.5$ s for DM linear forward trajectories (blue circles), DM linear backward trajectories (green circles), and all DM trajectories (black circle) obtained from a 3 min-video before ionomycin treatment. Figure 4s shows PDF plots for $\Delta r'$ from other time periods. The red fitting line is $P(\Delta r') = 0.3 \cdot e^{(-1.4|\Delta r'|)}$.

f. PDF Plots of $P(\Delta r')$ under the same conditions as in (g) obtained from a 3 min-video beginning 9 min after ionomycin administration. Star shows a clear rise in the backward distribution of $\Delta r'$.



Extend Data Fig.5. Time lapse plots of the probability density function (PDF) for instantaneous velocity P (Inst. Velocity) and PDF of normalized instantaneous displacement $\Delta r'$ for two representative cells after ionomycin administration. This figure is related to Fig. 4.

a. Plots of the probability density function (PDF) for instantaneous velocity of the DM trajectories (red circles), AD trajectories (blue circles), and all trajectories (green circles) obtained before and 5, 10, or 20 min after ionomycin administration. The red curve is the DM data fitted to a Gaussian curve, the blue line is the AD data fitted to an exponential curve, the green line is the data for all trajectories fitted to the DM and AD switch model. The (a) and (c) panels are from two different cells.

b. PDF Plots $P(\Delta r')$ for normalized instantaneous displacement $\Delta r'$ during the time lag $\tau = 6.5\text{s}$ for linear forward trajectories (blue circles), linear backward trajectories (green circles), and all trajectories (black circle) for DM trajectories obtained before and 5, 10, or 20 min after administration of ionomycin. PDF plots for $\Delta r'$ from other time periods are shown in Figure 4s. The red fitting line is $P(\Delta r') = 0.3 \cdot e^{(-1.4|\Delta r'|)}$. Data in (b) are from the same cell as in (a).

- c. The same color code as (a). Data of (c) are from another cell.
- d. The same color code as (b). Data of (d) are from the same cell as in (c).

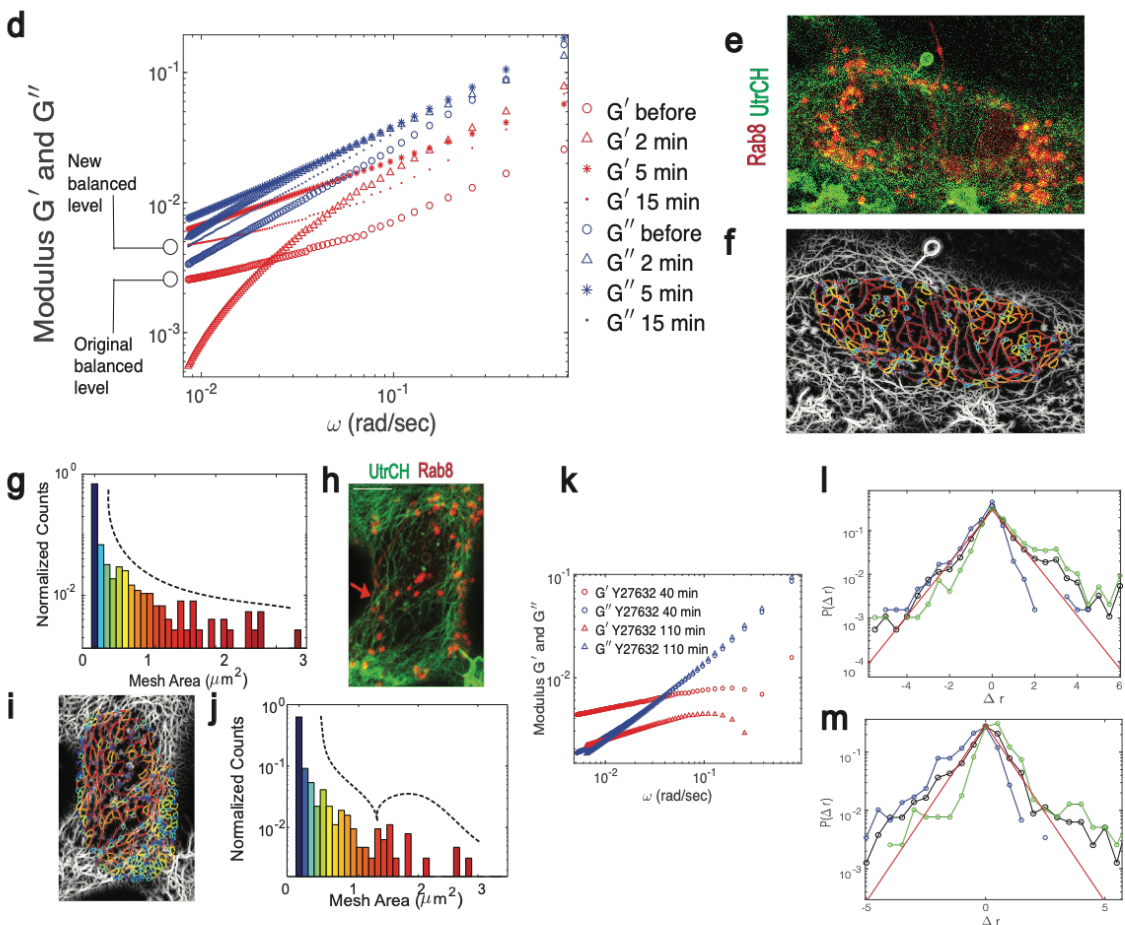
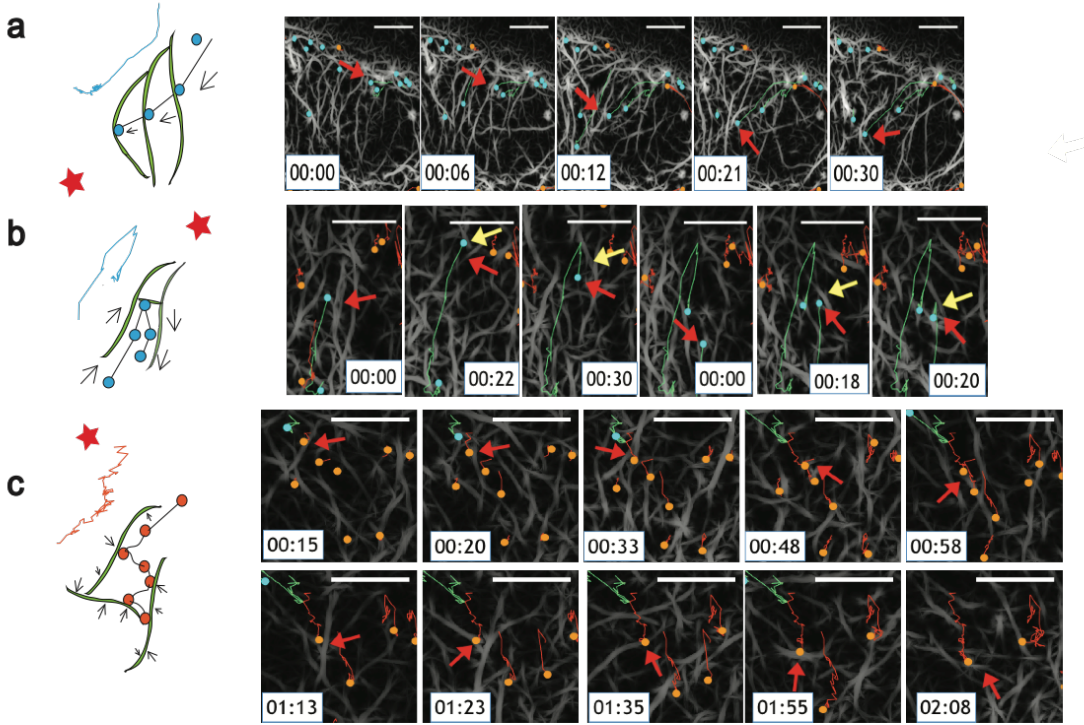
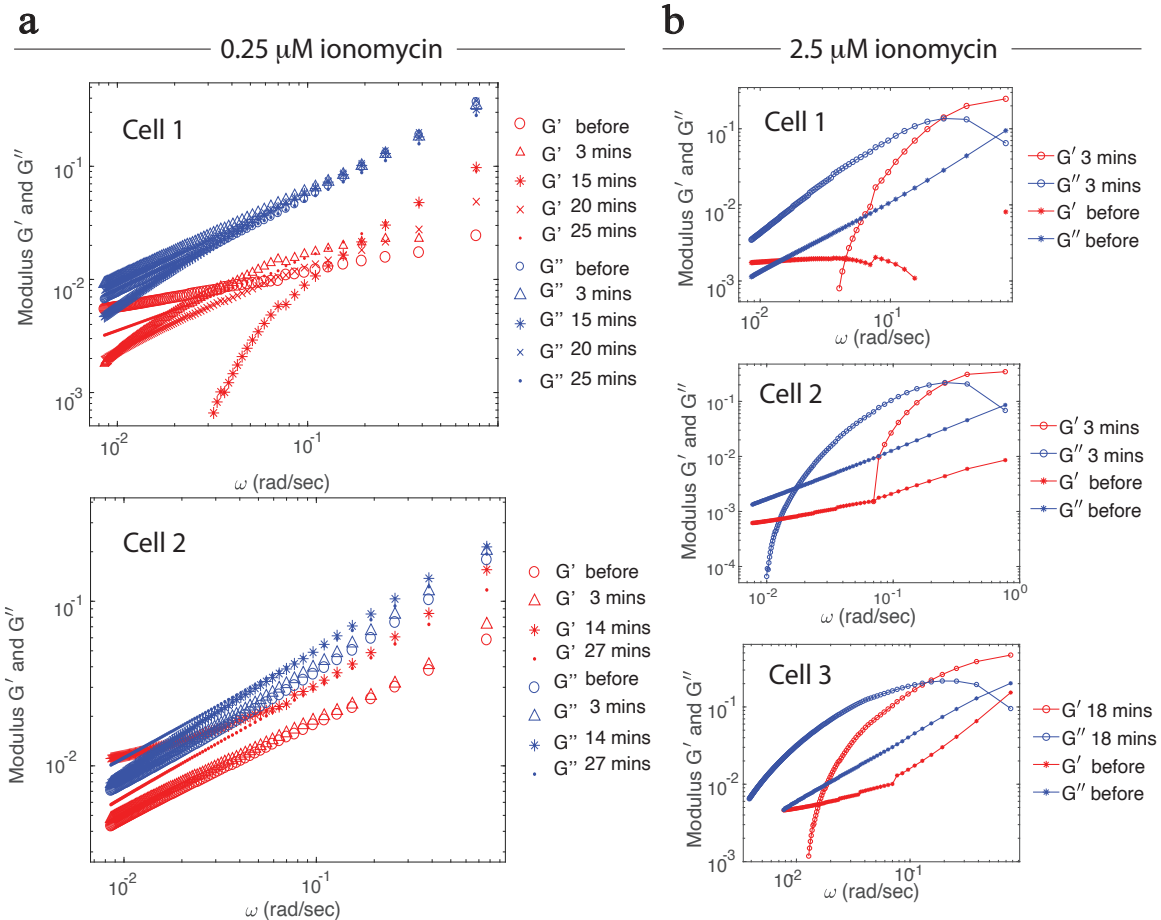


Fig. 5 Mechanical response of DDAM induced by flow

- a.** Left: Cartoon illustration of the interaction of a long actin fiber blocking transport of the vesicle to the primary cilia and producing the representative cyan trajectories shown above the cartoon. Cyan dots label the vesicle location, red star labels the cilia location, black arrows following the cyan dots show the amplitude and direction of the nearest cyan dots. Right: Time-lapse images of the overlay of enhanced actin fibers (grey) labeled by UtrCH-GFP and ciliary trafficking vesicles labeled by rab8-mCherry. Cyan circles label vesicles going toward cilia during the 5 min recording, orange circles label vesicles going away from cilia. A line of the same color attaches each vesicle to its trajectory. Red arrows point to the vesicle of interest over time. In this case, the force applied by the vesicle caused the actin fiber to bend, and the vesicle of interest stalled. The scale bar is 5 μm . The same color code applies to (b) and (c).
- b.** Left: Cartoon illustration of the actin fiber that causes the vesicle to bounce back from its direction of motion. Right: Because the fibers that cause the vesicles to bounce have a fast turnover rate, yellow errors are added to the image perpendicular to the fiber to show the location of their interaction with the vesicle.
- c.** Left: Cartoon illustration of diffuse vesicles constantly whipped by nearby actin fibers, resulting in a typical zig zag trajectory.
- d.** Plots of elastic (G' , red) and viscous (G'' , blue) moduli along with the frequency (ω) calculated for one cell before (circles) and 2 (triangles), 5 (stars), and 15 min (dots) after administration of 0.25 μM ionomycin. The two sets of curves labeled by G' and G'' before and 15 min after treatment are highlighted to show the rebalanced process of the mechanical responses.
- e.** Representative image of a ciliated hRPE1 cell transiently expressing Rab8-mCherry and UtrCH-GFP. Red arrows point to the base of the cilia.
- f.** Extracted actin mesh by OFT transformation from UtrCH channel. Single actin fiber is enhanced to show the mesh better than the raw image.
- g.** Distribution of the mesh sizes for the cell shown in (f). Dashed line is an arbitrary trend line drawn by the authors. The color code for the range of the mesh areas is the same as in (h).
- h.** Representative image of a ciliated hRPE1 cell transiently expressing Rab8-mCherry and **i.** UtrCH-GFP and its extracted branched actin meshes, after treatment with Y27632 ($n = 9$ cells, 3 independent experiments).
- j.** Distribution of the mesh sizes for the cell shown in (g).
- k.** Plots of elastic (G' , red) and viscous (G'' , blue) moduli along with the frequency (ω) calculated for two cells after 40 min (circles) and 110 min (triangles) of treatment with 1 μM Y27632.
- l.** PDF Plots $P(\Delta r')$ for normalized instantaneous displacement $\Delta r'$ during the time lag $\tau = 6.5\text{s}$ for DM linear forward trajectories (blue circles), DM linear backward trajectories (green circles), and all DM trajectories (black circle) obtained from a 3 min-video before Y27632 treatment. The red fitting line is $P(\Delta r') = 0.3 \cdot e^{(-1.4|\Delta r'|)}$.
- m.** PDF Plots of $P(\Delta r')$ under the same conditions as in (l) obtained from a 3 min-video beginning 40 min after Y27632 administration.



Extend Data Fig.6 Time lapse plots of the viscoelastic moduli after treatment with different doses of ionomycin. This figure is related to Fig. 5.

a. Plots of elastic (G' , red) and viscous (G'' , blue) moduli along with the frequency (ω) calculated for one cell before (circles) and 2 (triangles), 5 (stars), and 15 min (dots) after administration of $0.25\mu\text{M}$ ionomycin. This plot uses the same color code as Figure 5D, but the data are obtained from two different cells.

b. Plots of elastic (G' , red) and viscous (G'' , blue) moduli along with the frequency (ω) calculated for three cells before (circles) and after (stars) treatment with $2.5\mu\text{M}$ ionomycin.

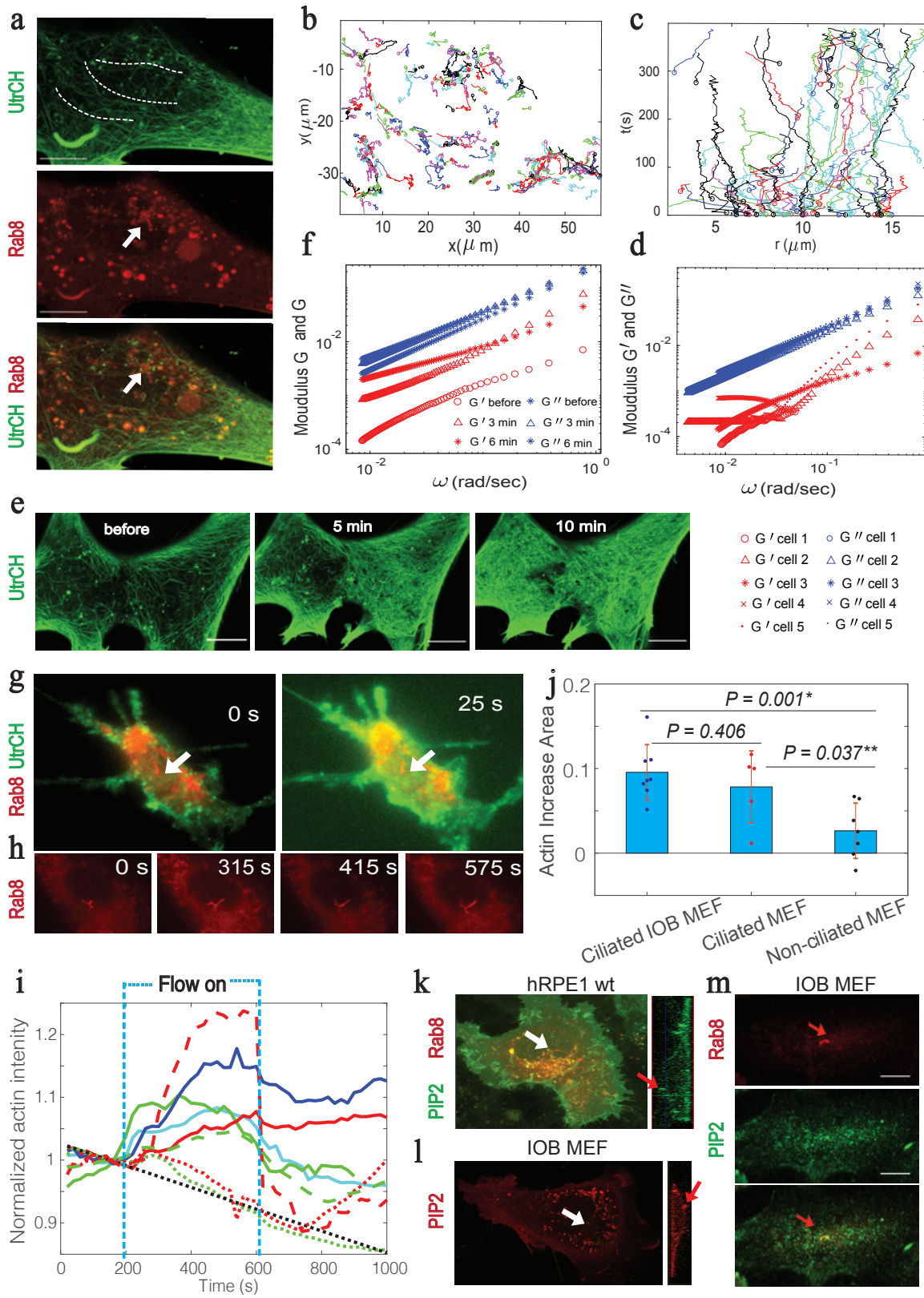


Fig. 6 PI(4,5)P₂ regulates depolymerization of DDAM

- a.** Representative image of an IOB MEF cell transiently expressing Rab8-mCherry and UtrCH-EGFP. The GFP channel shows an actin web structure spreading out around the nuclear region; the mCherry channel shows the Rab8-labeled vesicles and cilia. White arrow points to the base of the cilia, where vesicles remain crowded. Three dashed lines in the GFP channel show several actin fibers that persist through the whole recording. Supplemental video 6 shows the motion and dynamic interaction of vesicles and actin fibers in this cell ($n = 10$ cells, 6 independent experiments).
- b.** Single vesicle tracking trajectories obtained for the same cell shown in (e) from a 6 min video of Rab8-mCherry labeled vesicles recorded at 1.3s per frame. Each trajectory has a circle at the beginning to label its start location. The three red dashed lines are at the same location as in (e). The trajectories show that the vesicles are trapped along the persistent actin fibers.
- c.** Plots of the distance r between the vesicle and the ciliary base along with time t for all trajectories. Most trajectories demonstrate a small swing motion back and forth from cilia, the same feature as those trapped by the persistent actin fibers. The trajectory data are the same as in (f).
- d.** Plots of elastic (G' , red) and viscous (G'' , blue) moduli along with the frequency (ω) calculated for five cells in the quiescent state. The elastic modulus of the IOB MEF cells is obviously decreased compared to that of healthy cells.
- e.** Time-lapse images of a representative IOB MEF cell transiently expressing UtrCH-GFP and Rab8-mCherry before, 5 min and 10 min after treatment with 0.25uM ionomycin. Actin polymerization in IOB MEF cells is much more pronounced than in healthy cells.
- f.** Plots of elastic (G' , red) and viscous (G'' , blue) moduli along with the frequency (ω) calculated for one cell before (circles), 3 min (triangles), and 6 min (stars) after treatment with 0.25uM ionomycin.
- g.** Time-lapse images of a representative IOB MEF cell transiently expressing UtrCH-GFP and Rab8-mCherry before and 25s after applying flow. White arrow points to the base of the cilia ($n = 5$ cells, 2 independent experiments). See also supplemental video 6.
- h.** Time-lapse images of a representative cilia in IOB MEF cells responding to flow show that the cilia are branched and very flexible. Same dataset as in (a).
- i.** Branched actin polymerization of IOB MEF cells in response to flow. Normalized increase is plotted by the same method as in Figure 3C for ciliated IOB MEFs (solid lines, $n=8$, 4 independent experiments), ciliated wt MEFs (dashed lines, $n=5$, 4 independent experiments), and non-ciliated MEFs (dotted lines, $n=7$ cells, 3 independent experiments).
- j.** Statistics of the area covered in the flow chart shown in (b) for ciliated cells and non-ciliated cells. The area covered by the reference photo bleach line shown in orange is subtracted from the measured individual areas. The dots on the bar plot show the measured value of the individual areas ($n = 16$ cells, $p = 0.002$, 5 independent experiments).
- k.** Representative image of an hRPE1 cell transiently expressing Rab8-mCherry and PH-PLC- δ -CFP. Left: a single slice image focuses on a plane ~ 400-600nm from the bottom of the cell and 400nm in thickness. The white arrow points to the base of the cilia in the top view, and the red arrow points to the cilia location in the side view. Scale bar is 10 μ m ($n = 20$ cells, 3 independent experiments).
- l.** Representative image of an IOB MEF transiently expressing PH-PLC- δ -mCherry. Left: a single slice image focuses on a plane ~ 400-600nm from the bottom of the cell and 400nm in

thickness. The white arrow points to the base of the cilia, and the red arrow points to the cilia location in the side view. Scale bar is 10 μ m (n = 30 cells, 3 independent experiments).

m. Representative image of a fixed IOB MEF stained with PI(4,5)P₂ antibody and Arl13b antibody.

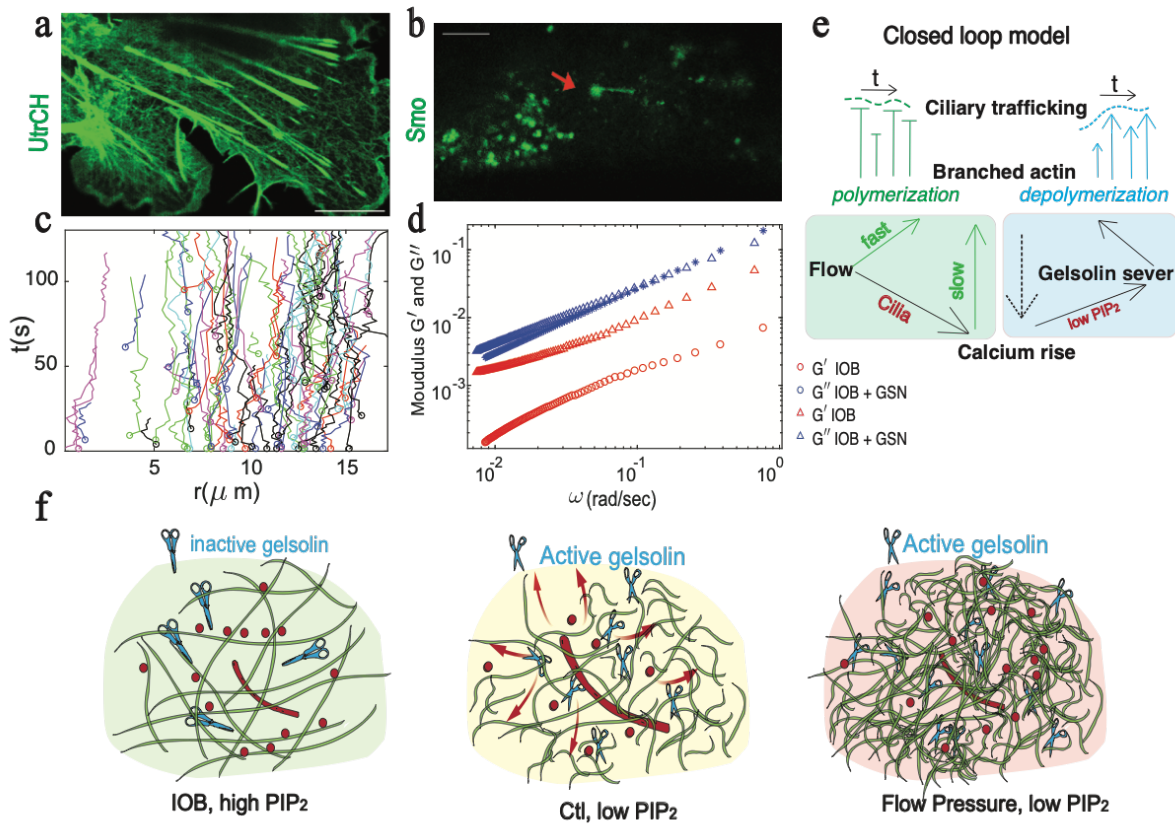


Fig. 7 Gelsolin as a feedback sensor of mechanosensation loop of DDAM

- a.** Rescue of the depolymerization of actin networks in an IOB MEF cell that transiently expresses UtrCH-GFP and GelsolinN-mCherry. Only the GFP channel is shown. Turnover of the cortical actin fibers becomes faster. Also see supplemental video 7.
- b.** Rescue of smo transportation to primary cilia in an IOB MEF cell that transiently expresses YFP-smo and GelsolinN-mCherry. Only the GFP channel is shown. Red arrow points to the base of the cilia. In this cell smo transport to cilia and the vesicle- clear region around the ciliary base and near the nucleus are restored and similar to that found in control cells. Scale bar is 10 μ m (n = 5 cells, 3 independent experiments). Also see supplemental video 7.
- c.** Plots of the distance r between the vesicle and the ciliary base along with time t for all trajectories obtained from the same cell as in (b). Collective backward motion is restored in the smo-marked vesicles.
- d.** Plots of elastic (G' , red) and viscous (G'' , blue) moduli along with the frequency (ω) calculated for one IOB MEF cell (circles) and one IOB MEF cell transiently transfected with gelsolinN (GSN). After introduction of GSN, the elastic modulus resembles that of control cells.
- e.** Close loop model of the mechanosensation of ciliary signaling.

f. Cartoon illustrations of the interaction between the branched actin network and ciliary trafficking vesicles in three scenarios in this study. In IOB MEF cells: High membrane content of PI(4,5)P₂ around cilia inhibits severing by gelsolin and defective depolymerization of F-actin networks traps the vesicles. Cilia are shortened as a result of reduced delivery of the ciliary trafficking vesicles. In control cells: fluctuation of the calcium and membrane content of PI(4,5)P₂ enables a balance between polymerization and depolymerization of branched actin networks and maintains dynamic control of the trafficking of ciliary trafficking vesicles. In control cells with extra flow pressure: flow triggers a higher level of calcium and polymerization of branched actin networks. Gelsolin is triggered later when calcium reaches its threshold for activation. Gelsolin accelerates depolymerization of F-actin and balances trafficking in response to the newly added flow pressure.

Supplemental Videos

Supplemental video 1. Collective exclusion of ciliary targeting vesicles. This video is related to Figure 1.

- a.** Time-lapse confocal images of an hRPE1 cell (Left) expressing Rab8-mCherry that labels cargo vesicles and cilia. The arrow points to the base of the cilia, and a MEF (right) expressing Rab8-mCherry that labels intracellular vesicles in a non-ciliated cell. Scale bar is 5 (Left) and 10 (right) μm . The time-lapse images are zoomed in for a better view of the retrograde motions of Rab8 vesicles in the left ciliated (arrows) and the local motion in the right non-dilated cell.
- b.** Time-lapse epic-fluorescence images of an hRPE1 cell steadily expresses IFT80-GFP that labels the cilia, and transiently expresses Arl13B- mCherry that labels cargo vesicles and cilia. The white arrow points to the retrograde motions of Arl13B vesicles. Scale bar is 5 μm .
- c.** Time-lapse epic-fluorescence images of an hRPE cell transiently expresses Rab8-mCherry and YFP-SMO that both label cargo vesicles and cilia. The white arrow points to the retrograde motions of Arl13B vesicles. Scale bar is 5 μm .
- d.** Time-lapse confocal images of an hRPE1 cell expressing Rab8-mCherry that labels cargo vesicles and cilia, and EB3-GFP labels the microtubules. The arrow points to the base of the cilia. Scale bar is 5 μm .

Supplemental video 2. Live cell actin labeling by UtrCH and Lifeact. This video is related to Figure 2.

- a.** Time-lapse confocal images of a ciliated hRPE1 cell (Left) and non-ciliated MEF (right) transiently expressing Rab8-mCherry and the UtrCH-EGFP. Scale bar is 10 μm . The time-lapse images are zoomed in for a better view of the single actin fiber turnover of DDAM in the ciliated cell and stable actin fiber in the non-ciliated cell.
- b.** Time-lapse confocal images of a ciliated hRPE1 cell transiently expressing Rab8-mCherry and the Lifeact-EGFP. Lifeact labeling shows no specific actin structures in the vesicle retrograde motion region.

Supplemental video 3. The response of DDAM/Ca²⁺ to fluid flow, the response of DDAM to Ca²⁺. This video is related to Fig. 3.

- a. Time-lapse epi-fluorescent images of an hRPE cell transiently expresses Rab8-mCherry and UtrCH-GFP in a sequence of “flow off- flow on- flow off” in the flow chamber. The scale bar is 10 μM.
- b. Time-lapse pseudo-color plot of calcium signal (Left) and epic-fluorescent images of Gcamp6f channel (right) of an hRPE cell transiently expresses Rab8-mCherry and GCamp6f-GFP in a sequence of “flow off- flow on- flow off” in the flow chamber. The scale bar is 10 μM.
- c. Time-lapse confocal fluorescent images of an hRPE cell transiently expresses Rab8-mCherry and UtrCH-GFP before (Left) and after 2 min (right) treatment of 0.25 μM ionomycin. The time-lapse images are zoomed in for a better view of the downsizing of the single meshes of DDAM due to polymerization.

Supplemental video 4. The response of DDAM to different concentrations of ionomycin. This video is related to Fig. 4.

- a. Time-lapse confocal fluorescent images of an hRPE cell transiently expresses Rab8-mCherry and UtrCH-GFP before (Left) and after 10 min (right) treatment of 0.25μM ionomycin. The time-lapse images are zoomed in for a better view of the DDAM polymerization after treatment.
- b. Time-lapse confocal fluorescent images of an hRPE cell transiently expresses Rab8-mCherry and UtrCH-GFP before (Left) and after 3 min (right) treatment of 2.5μM ionomycin. The time-lapse images are zoomed in for a better view of the DDAM polymerization and dissolve, and cilia disappear after treatment.

Supplemental video 5. The enhanced DDAM shows the interaction between a single actin fiber and a cargo vesicle. This video is related to Figure 5.

Time-lapse confocal fluorescent images (Left) and the enhanced images (right) of an hRPE cell transiently expresses Rab8-mCherry and UtrCH-GFP. The vesicles on the right images are labeled for “to cilia” (cyan) and “away cilia” (orange) to show the pattern explained in figure 5.

Supplemental video 6. Single fiber turnover of DDAM in IOB and wt MEF, and the cilia of IOB MEF to the flow. This video is related to Figure 6.

- a. Time-lapse confocal images of a ciliated IOB MEF (Left) and wt MEF (right) transiently expressing Rab8-mCherry and the UtrCH-EGFP. Scale bar is 10 μm. The time-lapse images are zoomed in for a better view of the slow single actin fiber turnover of DDAM in the IOB MEF and the fast turnover in a wt MEF.
- b. Time-lapse epic-fluorescent images of an IOB MEF transiently expresses Rab8-mCherry and UtrCH-GFP in a sequence of “flow off- flow on- flow off” in the flow chamber. Rab8 labeled cilia in mCherry channel shows cilia branch behaviors. The scale bar is 10 μM.

Supplemental video 7. The rescue of SMO trafficking to cilia and DDAM dynamics by gelsolinN. This movie is related to Figure 7.

- a. Time-lapse confocal images of a ciliated IOB MEF transiently expressing gelsolinN-mCherry and the SMO-YFP. Scale bar is 10 μm.
- b. Time-lapse confocal images of a ciliated IOB MEF transiently expressing gelsolinN-mCherry and the UtrCH-GFP. The time-lapse images are zoomed in for a better view of the rapid single

actin fiber turnover of DDAM in the IOB MEF after the transfection of gelsolinN. Scale bar is 10 μ m.

References

1. Vining, K.H. & Mooney, D.J. Mechanical forces direct stem cell behaviour in development and regeneration. *Nature Reviews Molecular Cell Biology* **18**, 728 (2017).
2. He, L., Si, G., Huang, J., Samuel, A.D.T. & Perrimon, N. Mechanical regulation of stem-cell differentiation by the stretch-activated Piezo channel. *Nature* **555**, 103 (2018).
3. Aragona, M. *et al.* A Mechanical Checkpoint Controls Multicellular Growth through YAP/TAZ Regulation by Actin-Processing Factors. *Cell* **154**, 1047-1059 (2013).
4. Panciera, T., Azzolin, L., Cordenonsi, M. & Piccolo, S. Mechanobiology of YAP and TAZ in physiology and disease. *Nature Reviews Molecular Cell Biology* **18**, 758 (2017).
5. Singla, V. & Reiter, J.F. The Primary Cilium as the Cell's Antenna: Signaling at a Sensory Organelle. *Science* **313**, 629 (2006).
6. Goetz, S.C. & Anderson, K.V. The primary cilium: a signalling centre during vertebrate development. *Nature Reviews Genetics* **11**, 331-344 (2010).
7. Ishikawa, H. & Marshall, W.F. Ciliogenesis: building the cell's antenna. *Nature Reviews Molecular Cell Biology* **12**, 222-234 (2011).
8. Ford, M.J.Y., Patricia L.; Mali, Girish R.; Keighren, Margaret A.; Waddell, Scott H.; Mjoseng, Heidi K.; Douglas, Adam T.; Hall, Emma A.; Sakaue-Sawano, Asako; Miyawaki, Atsushi; Meehan, Richard R.; Boulter, Luke; Jackson, Ian J.; Mill, Pleasantine; Mort, Richard L. A Cell/Cilia Cycle Biosensor for Single-Cell Kinetics Reveals Persistence of Cilia after G1/S Transition Is a General Property in Cells and Mice. *Developmental Cell* **47** (2018).
9. Phua, S.C. *et al.* Dynamic Remodeling of Membrane Composition Drives Cell Cycle through Primary Cilia Excision. *Cell* **168**, 264-279.e215 (2017).
10. Praetorius, H.A. & Spring, K.R. Bending the MDCK Cell Primary Cilium Increases Intracellular Calcium. *The Journal of Membrane Biology* **184**, 71-79 (2001).
11. Praetorius, H.A. & Spring, K.R. Removal of the MDCK Cell Primary Cilium Abolishes Flow Sensing. *The Journal of Membrane Biology* **191**, 69-76 (2003).
12. Delling, M., DeCaen, P.G., Doerner, J.F., Febvay, S. & Clapham, D.E. Primary cilia are specialized calcium signalling organelles. *Nature* **504**, 311 (2013).
13. Delaine-Smith, R.M., Sittichokechaiwut, A. & Reilly, G.C. Primary cilia respond to fluid shear stress and mediate flow-induced calcium deposition in osteoblasts. *The FASEB Journal* **28**, 430-439 (2013).
14. Janmey, P.A. & McCulloch, C.A. Cell Mechanics: Integrating Cell Responses to Mechanical Stimuli. *Annual Review of Biomedical Engineering* **9**, 1-34 (2007).
15. Nauli, S.M. *et al.* Polycystins 1 and 2 mediate mechanosensation in the primary cilium of kidney cells. *Nature Genetics* **33**, 129-137 (2003).
16. Brennan, C., Mangoli, M., Dyer, C.E.F. & Ashworth, R. Acetylcholine and calcium signalling regulates muscle fibre formation in the zebrafish embryo. *Journal of Cell Science* **118**, 5181 (2005).
17. Nonaka, S., Shiratori, H., Saijoh, Y. & Hamada, H. Determination of left-right patterning of the mouse embryo by artificial nodal flow. *Nature* **418**, 96-99 (2002).

18. Yoshiba, S. *et al.* Cilia at the Node of Mouse Embryos Sense Fluid Flow for Left-Right Determination via Pkd2. *Science* **338**, 226 (2012).
19. Delling, M. *et al.* Primary cilia are not calcium-responsive mechanosensors. *Nature* **531**, 656 (2016).
20. He, W. *et al.* Dynamic heterogeneity and non-Gaussian statistics for acetylcholine receptors on live cell membrane. *Nature Communications* **7**, 11701 (2016).
21. Kovacs, J.J. *et al.* β -Arrestin–Mediated Localization of Smoothened to the Primary Cilium. *Science* **320**, 1777 (2008).
22. He, M., Agbu, S. & Anderson, K.V. Microtubule Motors Drive Hedgehog Signaling in Primary Cilia. *Trends in Cell Biology* **27**, 110-125 (2017).
23. Yan, X. & Zhu, X. Branched F-actin as a negative regulator of cilia formation. *Experimental Cell Research* **319**, 147-151 (2013).
24. Kim, J. *et al.* Actin remodelling factors control ciliogenesis by regulating YAP/TAZ activity and vesicle trafficking. *Nature Communications* **6**, 6781 (2015).
25. Drummond, M.L. *et al.* Actin polymerization controls cilia-mediated signaling. *The Journal of Cell Biology* **217**, 3255 (2018).
26. Bieling, P. *et al.* Force Feedback Controls Motor Activity and Mechanical Properties of Self-Assembling Branched Actin Networks. *Cell* **164**, 115-127 (2016).
27. Mueller, J. *et al.* Load Adaptation of Lamellipodial Actin Networks. *Cell* **171**, 188-200.e116 (2017).
28. Dong, R. *et al.* Endosome-ER Contacts Control Actin Nucleation and Retromer Function through VAP-Dependent Regulation of PI4P. *Cell* **166**, 408-423 (2016).
29. Daste, F. *et al.* Control of actin polymerization via the coincidence of phosphoinositides and high membrane curvature. *The Journal of Cell Biology* **216**, 3745 (2017).
30. Lee, S., Tan, H.Y., Geneva, I.I., Kruglov, A. & Calvert, P.D. Actin filaments partition primary cilia membranes into distinct fluid corrals. *The Journal of Cell Biology* **217**, 2831 (2018).
31. Riedl, J. *et al.* Lifeact: a versatile marker to visualize F-actin. *Nature Methods* **5**, 605 (2008).
32. Burdyniuk, M., Callegari, A., Mori, M., Nédélec, F. & Lénárt, P. F-Actin nucleated on chromosomes coordinates their capture by microtubules in oocyte meiosis. *The Journal of Cell Biology* **217**, 2661 (2018).
33. Chatila, T., Silverman, L., Miller, R. & Geha, R. Mechanisms of T cell activation by the calcium ionophore ionomycin. *The Journal of Immunology* **143**, 1283 (1989).
34. Sandberg, K. & Brega, M. Segmentation of thin structures in electron micrographs using orientation fields. *Journal of Structural Biology* **157**, 403-415 (2007).
35. Zhang, Z., Nishimura, Y. & Kanchanawong, P. Extracting microtubule networks from superresolution single-molecule localization microscopy data. *Molecular Biology of the Cell* **28**, 333-345 (2016).
36. Hoffman, B.D., Massiera, G., Van Citters, K.M. & Crocker, J.C. The consensus mechanics of cultured mammalian cells. *Proceedings of the National Academy of Sciences* **103**, 10259 (2006).
37. Gardel, M.L., Valentine, M.T., Crocker, J.C., Bausch, A.R. & Weitz, D.A. Microrheology of Entangled F-Actin Solutions. *Physical Review Letters* **91**, 158302 (2003).

38. Gardel, M.L. *et al.* Scaling of F-Actin Network Rheology to Probe Single Filament Elasticity and Dynamics. *Physical Review Letters* **93**, 188102 (2004).
39. De Matteis, M.A., Staiano, L., Emma, F. & Devuyst, O. The 5-phosphatase OCRL in Lowe syndrome and Dent disease 2. *Nature Reviews Nephrology* **13**, 455 (2017).
40. Larson, L. *et al.* Gelsolin mediates calcium-dependent disassembly of Listeria actin tails. *Proceedings of the National Academy of Sciences of the United States of America* **102**, 1921 (2005).
41. Janmey, P.A. & Stossel, T.P. Modulation of gelsolin function by phosphatidylinositol 4,5-bisphosphate. *Nature* **325**, 362-364 (1987).
42. Sun, H.Q., Yamamoto, M., Mejillano, M., Yin, H.L. & ‡ Gelsolin, a Multifunctional Actin Regulatory Protein. *Journal of Biological Chemistry* **274**, 33179-33182 (1999).
43. Cooper, J.A. *et al.* Microinjection of gelsolin into living cells. *The Journal of Cell Biology* **104**, 491 (1987).
44. Nagaya, H. *et al.* Regulated motion of glycoproteins revealed by direct visualization of a single cargo in the endoplasmic reticulum. *The Journal of Cell Biology* **180**, 129 (2008).
45. Prosseda, P.P. *et al.* Loss of OCRL increases ciliary PI(4,5)P₂; in Lowe oculocerebrorenal syndrome. *Journal of Cell Science* **130**, 3447 (2017).
46. Luo, N. *et al.* Primary cilia signaling mediates intraocular pressure sensation. *Proc Natl Acad Sci U S A* **111**, 12871-12876 (2014).
47. Shao, X., Li, Q., Mogilner, A., Bershadsky, A.D. & Shivashankar, G.V. Mechanical stimulation induces formin-dependent assembly of a perinuclear actin rim. *Proceedings of the National Academy of Sciences* **112**, E2595 (2015).

Methods

Mice

All experiments involving mice followed the guidelines of the Association for Research in Vision and Ophthalmology Statement for the Use of Animals in Ophthalmic and Vision Research and were approved by the Institutional Animal Care and Use Committee (IACUC) of Stanford University School of Medicine.

Wild-type mouse lines C57BL/6 were obtained from the Jackson Laboratories, and the Ocrl-/- and Ocrl-/- Inpp5b-/- INPP5B+/+ (IOB) mice were a gift from Robert L. Nussbaum lab in University of California, San Francisco. Both mouse species are housed under 12-hour light/dark cycles with access to water and food.

Cell culture and drug treatment

The hTERT RPE1 (hRPE1, gift from Peter K. Jackson lab) cells were cultured in DMEM medium (Corning, No. 10-017-CV) containing 10% FBS. The primary MEFs were derived from E14.5 wild type/ IOB mouse without brain, limbs, or internal organs and washed with sterile PBS, minced into small pieces with a sterile razor blade, digested with trypsin in 37°C for 15 min, homogenized by pipetting, and plated in a 10 cm dish with DMEM and 15% FBS. In all experiments, cells were cultured in the starvation medium for 24 -48 hrs to induce ciliogenesis. The starvation medium was DMEM containing 0%- 0.1% FBS. In the non-flow chamber experiment, the cells were seeded on glass bottom chambers (Greiner Bio-One, No. 627870) coated with fibronectin (EMD Millipore, No. FC010). Drug treatment was performed with 7nM latrunculin B (Sigma-Aldrich, No. L5288-1MG), 1μM Y27632 (Fisher Scientific, No. 50175996), 0.25μM, and 2.5μM ionomycin (MP Biomedicals, No. 15507001).

Transfection

For the transient transfection, cells were seeded in glass bottom chambers for 24 hrs and then transfected with the respective DNA plasmids by Lipofectamine™ 3000 Transfection Reagent (Thermo Fisher, No. L3000015). Plasmids used in this work: Rab8-mCherry, YFP-smo, Arl13b-mCherry (Gift from Tim Stearns Lab), PLC(PH)-D1-CFP(for PIP₂) (Gift from Robert Stahelin

Lab), pGP-CMV-GCaMP6f, Ezrin-EGFP, Lifeact-GFP, Utro-CH-EGFP, Ch-gelsolN and EB3-mTurquoise2 (Addgene, No. 40755, 20681, 58470, 26737, 37262, 98825).

Immunofluorescence

To detect cilia and F-actin in fixed cells, the cells were grown on glass bottom chambers at 70-80% confluence and ciliogenesis induced in starvation medium for 24-48 hrs. The cells were then treated with 4% (v/v) paraformaldehyde at room temperature for 15 mins, and permeabilized by 0.1% Triton X-100 for 5min. For staining of the cilia, the permeabilized cells were blocked with 2% bovine serum albumin for 1 hr at room temperature, treated with Anti-ARL13B rabbit polyclonal antibody (Proteintech, NO. 17711-1-AP, 1:200) for 1 hr at room temperature, washed three times, then treated with the secondary antibody. For staining of F-actin, the permeabilized cells were treated with Phalloidin-Alexa 488 (Fisher Scientific, No. A12379).

To detect PIP2 in fixed cells, the cells were fixed and stained as in published protocols¹. The cells were grown on 8-well chamber slides (Thermo Fisher, No. 177402PK) to 70%- 80% confluence and ciliogenesis induced with starvation medium for 24-48 hrs. The cells were then treated with 2% (v/v) paraformaldehyde at room temperature for 15 mins, permeabilized by 20uM digitonin for 5min in buffer A, blocked with buffer A for 1 hr at room temperature, and treated with anti-PIP2 antibody (Abcam, No. ab11039, 1:200) for 90min at room temperature. After three washes with buffer A, the secondary antibody and anti-ARL13B rabbit polyclonal antibody (Proteintech, No. 17711-1-AP, 1:200) were added for 1 hr at room temperature. After three washes with buffer A, the cells were treated with a secondary antibody of another color, post-fixed with 2% PFA for 5min, washed twice with FBS containing 50mM NH4Cl and once with distilled deionized water.

Epi-fluorescent imaging

Live cells were cultured in a glass-bottom chamber to 70%-80% confluence and transfected with specific DNA plasmids. After ciliogenesis was induced by starvation medium for 24- 48 hrs, the culture medium was changed to pre-heated phenol red (P/R) free DMEM (Corning, No. 17-205-CV). Images were acquired with an Axio Observer Z1 inverted (Zeiss) microscope with a 63X oil objective equipped with an ORCA-Flash4.0 LT Digital CMOS camera (Hamamatsu). Time-lapse

imaging was performed at 500ms intervals for 1 -3 min per cell and obtained by Zeiss Zen software.

Confocal imaging

To examine the trafficking characteristics of vesicles targeted to cilia, we investigated a ciliary membrane protein, smoothened (SMO), and two small GTPases, ARL13B and Rab8. We tagged the proteins with fluorescent protein markers that were transiently transfected to human retinal pigmented epithelial (hRPE1) cells and MEFs. Live cells were prepared as described for epifluorescent imaging, and images acquired using a LSM800 confocal microscope (Zeiss) with a Plan-Aprochromat 63X oil objective lens (NA 1.4) and processed using Zeiss Zen software. In the setting shown in Extended Data Fig.2c, we obtained a large number of cargo vesicles and cilia in the single color channel within the thickness of a ~400 nm focus plane in the z-direction covering the ciliary base. Each cell is usually imaged before and after drug treatment as a Z-stack covering the whole cell and several time-lapse images. Time-lapse images are recorded ~400-nm above the glass bottom and include the vesicles and ciliary base. Each recording is 1.3~ 2.5s per frame for 4~ 7 min.

Single vesicle tracking

A custom MATLAB (2017b, The MathWorks) program based on the single-particle tracking algorithm² was used to obtain the position $\mathbf{r}(t)$ of an individual vesicle in a single frame t , and the trajectory of the vesicle constructed by linking the positions identified as belonging to the same vesicle over time. Several adaptions increased tracking accuracy. We revised the previous protocol³ and carried out the single vesicle tracking according to the following procedures:

- 1) Reducing noise of the raw image. The background of the fluorescent protein- labeled cell is quite noisy because of autofluorescence of the live cell and unbound fluorescent proteins. The gain of the camera/photomultiplier tubes (PMTs) also produces the entire image background. However, the size of the whole cell autofluorescence is much larger than the size of the vesicles, and the size of the dark current by the high camera/PMT gain is much smaller than the vesicle. We thus applied a band-pass filter to the raw image and subtracted a constant intensity threshold from each image. We noticed that the single vesicle

photobleached very quickly. As a result, we calculated the average intensity bleach curve for each video and fitted the curve with an exponential function. We then adjusted the intensity threshold according to the average intensity bleach function.

- 2) Setting the segmentation mask for the region of interest, excluding the cilia. After the de-noise in step 1), we found there are still irregular shapes labeled by the fluorescent protein markers, especially at the cell boundary. We next define the segmentation mask for the region of interest for tracking, which is an area that covers the nuclear region of the cell and around ~ 15 um in diameter in the center of the ciliary base. We also exclude the area covered by cilia from the mask because the linear-shaped bright cilia will introduce errors in vesicle recognition. The mask is generated in MATLAB using the Image Segmenter app.
- 3) Determining the location of the vesicle. The precise coordinates of the vesicle are determined from fitting the center of the cross-correlation matrix between the processed image and an isotropic 11 x 11 standard Gaussian kernel matrix.
- 4) Performing the single-vesicle tracking with the nearest neighbor algorithm². The algorithm requires the empirically selected threshold for the searching radius r . The value of r is determined by an average of half the distance between vesicles. The position of the vesicle in the next frame is determined by the nearest location within the distance r . This search of next location of the vesicle applied to the frame range of the next 1-5 frames. If no vesicles appear in the following five frames, the vesicle is considered as lost.
- 5) Manually adjust the missed-linked trajectories. The cargo vesicles exhibit tremendous heterogeneity in their luminosities, moving speeds and density in distribution. These characteristics produced a lot of tracking errors in the nearest neighbor algorithm. To correct the missed linked trajectories, we supplement the trajectories from step 5 with further manual correction. A set of MATLAB code is developed to break the trajectories, add new positions to the trajectories, exchange trajectories segments between two trajectories, or delete positions of the trajectories. A final collection of the trajectories is evaluated by the overlay of the trajectories with the vesicles in the raw image.

Trajectory segmentation

To obtain the directed motion (DM) and anomalous diffusion (AD) segments of the trajectories. We first calculated the aspect ratios (AR) of each trajectory by fitting them in an ellipse that covers the whole trajectories. The AR is then obtained by the ratio of short arm versus long arm. In an ideal circle, the AR =1. We defined the trajectories with AR< 0.5 linear trajectories. After carefully checking the linear trajectories that we regard as motor directed trajectory, we found that there are diffusion style segments in these trajectories (Fig. 4b). To exclude these diffusive segments and obtained pure motor directed segments, we developed a custom made segmentation algorithm with MATLAB based on a previously described algorithm⁴. To perform the segmentation, we plotted the trajectories with AR < 0.5 to a raw image of the cell where the trajectories are obtained. The resulted segment of pure DM is selected by hand and labeled by a marker to positions to those fragments. The DM fragments are extracted from the marked positions, while the rest of the trajectories are regarded as the AD segments.

Flow chamber imaging

Before imaging, the live-cells are prepared the same as introduced as in epi-fluorescent imaging. The image acquisition is then preformed using automated, inverted Zeiss Axio Observer 7 Marianas™ Microscope equipped with an X-Cite 120LED Boost White Light LED System and a high-resolution Prime™ Scientific CMOS digital camera that is controlled by a workstation loaded with SlideBook, an imaging and microscope control software (Intelligent Imaging Innovations, Inc.). Cells were washed twice before imaging in PBS and perfused during imaging with Tyrode solution (137 mM NaCl, 2.7 mM KCl, 1 mM MgCl₂, 2 mM CaCl₂, 0.2 mM Na₂HPO₄, 12 mM NaHCO₃, 11 mM D-glucose, 25 mM HEPES, 1% BSA) at room temperature (23-25°C) in a perfusion chamber (Warner Instruments, No. RC-21B). The bath solution was exchanged by a peristaltic pump (Harvard Apparatus) perfusion at a speed of 2 ml/min. During live-cell imaging, the exposure time for acceptor and donor channels was 100 ms, and images were collected every 10 s. The baseline was read for 5 min. All imaging processing was performed using Slidebooks software.

For each cell, we typically measured the period of 600s: the first 200s for baseline, the following 200s with the flow, and the last 200s for relaxation. The relaxation period is to test whether the

signals change after the flow is stopped. Because the fluorescent signals of DDAM are quite weak due to the deletion of the actin, we recorded at the plane of the ciliary base.

Quantification of the fluorescent intensity increase

To obtain the increase of the branched actin after the flow speed change from 0 to 2ml/min, we calculated the area from the flow chart as shown in Fig. 3c and subtracted the area from the area calculated from a reference photo-bleach line as shown in black dotted line in Fig. 3b. The reference photo-bleach line is determined from fitting the linear curve in the 100s-200s for one selected curve. The selection of the curve is empirical. Finally, to calculate the change of the fluorescence due to the flow speed change, we normalized the calculated change by dividing the area under the reference photo-bleach. This will give us a ratio of increase in comparison to the nature bleach line in imaging. This data will produce the data points as shown in Fig. 3c. A similar increase of the Ca^{2+} after flow is calculated in the same method to produce data points as shown in Fig. 3e, f.

To calculate the fluorescent increase in the flow chamber experiment, we first identify the DDAM region in the individual cells. Because the flow chamber imaging is epi-fluorescent microscope setting, DDAM signal is often buried by other actin filaments. In this case, we will select an empirical region around the nucleus shown by the cilia marker (Rab8-mCherry) channel. We then calculate the absolute intensity in the actin marker (UtrCH-GFP) channel. On a single frame, the absolute intensity of the GFP channel G_{ab} is calculated by the average intensity of the GFP intensity subtracted by the average intensity of the GFP intensity of an arbitrarily defined background area. In the case that we recorded both GFP and mCherry channels, we calculated the absolute intensity of the mCherry channel R_{ab} from intensity ratios from the same corresponding regions.

To obtain the increase of the branched actin in time-lapse after treatment of ionomycin, we obtained G_{ab} labeled by UtrCH-GFP and R_{ab} labeled by Rab8-mCherry. To compare the relative increased intensity from different cells along the time, we normalized G_{ab} with the fifth data point of pre-ionomycin (G_{ab0} (5)). To exclude the possibility that the cell may produce an increase of G_{ab} because of a non-specific auto-fluorescent in all channels instead of the response to flow. We

divided the resulted G_{abN} by R_{abN} as the increased intensity in G_{ab} through the time lapse recording produced a flow chart plotted in examples as in Fig. 3h and Extended Data Fig.4b,c.

Actin fiber enhancement and extraction of mesh sizes

Using live-cell actin labeling peptides, Lifeact, and the calponin homology domain of utrophin (UtrCH), we examined actin structures in hRPE1 cells and MEFs. To enhance the actin fibers in the DDAM because of the blur due to the weak signal and the high turnover rate, we applied the Line Filter Transform (LFT) and the Orientation Filter Transform (OFT) based on an algorithm reported previously^{5,6}. To extract the mesh size, we first apply a segmentation mask for the region of interest for mesh extraction. The area of mesh extraction overlaps with the region of the vesicle tracking. The mask is generated in MATLAB using the Image Segmenter app. We then transfer the resulted segmented image into a binary image by the Sauvola binarization⁷. On the produced binary Image, we applied the morphological operations to extract the skeleton of the mesh. The resulted mesh area distribution we plotted in Fig.5g, j is calculated by the histogram of the areas surrounded by every boundary in the skeleton.

Microrheology measurement of the elastic and viscous modules

To calculate the elastic and viscous modules from microrheology, we used the algorithm reported previously⁸. To process the segmented AD fragments of the trajectories, we used the GDL (GRAPHISOFT) based programs to first calculated the mean square displacement of the trajectories and then the viscoelastic moduli.

Method Reference

- 1 De Leo, M. G. *et al.* Autophagosome–lysosome fusion triggers a lysosomal response mediated by TLR9 and controlled by OCRL. *Nature Cell Biology* **18**, 839, doi:10.1038/ncb3386 <https://www.nature.com/articles/ncb3386#supplementary-information> (2016).
- 2 Crocker, J. C. & Grier, D. G. Methods of Digital Video Microscopy for Colloidal Studies. *Journal of Colloid and Interface Science* **179**, 298-310, doi:<https://doi.org/10.1006/jcis.1996.0217> (1996).
- 3 He, W. *et al.* Dynamic heterogeneity and non-Gaussian statistics for acetylcholine receptors on live cell membrane. *Nature Communications* **7**, 11701, doi:10.1038/ncomms11701 <https://www.nature.com/articles/ncomms11701#supplementary-information> (2016).

- 4 Helmuth, J. A., Burckhardt, C. J., Koumoutsakos, P., Greber, U. F. & Sbalzarini, I. F. A novel supervised trajectory segmentation algorithm identifies distinct types of human adenovirus motion in host cells. *Journal of Structural Biology* **159**, 347-358, doi:<https://doi.org/10.1016/j.jsb.2007.04.003> (2007).
- 5 Sandberg, K. & Bregå, M. Segmentation of thin structures in electron micrographs using orientation fields. *Journal of Structural Biology* **157**, 403-415, doi:<https://doi.org/10.1016/j.jsb.2006.09.007> (2007).
- 6 Zhang, Z., Nishimura, Y. & Kanchanawong, P. Extracting microtubule networks from superresolution single-molecule localization microscopy data. *Molecular Biology of the Cell* **28**, 333-345, doi:[10.1091/mbc.e16-06-0421](https://doi.org/10.1091/mbc.e16-06-0421) (2016).
- 7 Mustafa, W. A. & Abdul Kader, M. M. M. Binarization of Document Image Using Optimum Threshold Modification. *Journal of Physics: Conference Series* **1019**, 012022, doi:[10.1088/1742-6596/1019/1/012022](https://doi.org/10.1088/1742-6596/1019/1/012022) (2018).
- 8 Crocker, J. C. *et al.* Two-Point Microrheology of Inhomogeneous Soft Materials. *Physical Review Letters* **85**, 888-891, doi:[10.1103/PhysRevLett.85.888](https://doi.org/10.1103/PhysRevLett.85.888) (2000).

Acknowledgments

We thank Dr. Tia J. Kowal for critical reading of the manuscript. This work was supported by K08-EY022058 (Y.S.), R01-EY025295 (Y.S.), VA merit CX001298 (Y.S.), Ziegler Foundation for the Blind (Y.S.), R01EY026766 (M.S.K) and R01EY031167 (M.S.K). Children's Health Research Institute Award (Y.S.). Research for Prevention of Blindness Unrestricted grant (Stanford Ophthalmology), American Glaucoma Society (Y.S.), Lowe syndrome association (Y.S.), and Knights Templar Eye Foundation (Y.S.). P30 Vision Center grant to Stanford Ophthalmology department. Y.S. is a Laurie Kraus Lacob Faculty Scholar in Pediatric Translational Medicine.

Author Contributions

W. H., B.W. and Y.S. planned the research. W.H. performed all the experiments and data analysis. T.B. performed calcium imaging. W.H. B.W., and M.S.K wrote and revised the manuscript.

Declaration of Interests

The authors declare no competing financial interests.

Data and Code Availability

The data that support the findings of this study (such as figure source data) are available from the corresponding author (Y.S.) upon request. The MATLAB code for single vesicle tracking we used in this study is uploaded on GitHub (<https://github.com/hewei2017/Matlab-Vesicle-Tracking.git>)

Supplemental information:

The directed motion and anomalous diffusion switch model

In the biological system, the dynamics of unbound molecules are influenced by both the intracellular activities and the thermal agitation. Revealing the composition of the active transport from these mixed dynamics would lead to the characterization of the undetected force. The single-particle tracking technique is capable of characterizing the motor directed motions through the details of the trajectories of the molecules, and separate active transport from random thermal driven Brownian motion^{1,2}. In a single particle tracking study of the transmembrane protein acetylcholine receptor (AChR) on the live cell membrane, it has been reported that the probability of density function (PDF) $P(\Delta x')$ (and $P(\Delta y')$) in different time lag and other conditions collapse into a master fitting line of the exponential $P(\Delta x') = 0.3 \exp(-1.4|\Delta x'|)$. While $P(\Delta x')$ is measured from the instantaneous displacement of the $\Delta x(\tau)$ in the duration of $\tau = 4$ s, as a function of the normalized variables $\Delta x = \Delta x/(2D_l\tau)^{1/2}$, where $(2D_l\tau)^{1/2}$ is the average diffusion length, and D_l is the long-time diffusion coefficient of all linear vesicles. In a pure Brownian motion case, for example, the colloid beads, the measured $P(\Delta x')$ (and $P(\Delta y')$) would be Gaussian distribution according to the central limit theorem.

This dynamic heterogeneity and breaking of the central limit theorem revealed that the dynamics of the transmembrane proteins are influenced by the active and slow remodeling of cortical actin¹. In Fig. 1i, we have shown that the same dynamic heterogeneity applied to the intracellular vesicle trafficking to the primary cilia in our tracking region of interest. Here we measured the \mathbf{r} as the displacement of the vesicle regarding cilia. The probability of density function (PDF) $P(\Delta r')$ of the instantaneous displacement of the $\Delta r(\tau)$ in the duration of $\tau = 7.5$ s, as a function of the normalized variables $\Delta r' = \Delta r/(4D_l\tau)^{1/2}$, where $(4D_l\tau)^{1/2}$ is the average diffusion length, and D_l is the long-time diffusion coefficient of all linear vesicles. Noticeably, the probability of density function (PDF) $P(\Delta r')$, although mostly collapsed into the master curve of $P(\Delta r') = 0.3 \exp(-1.4|\Delta r'|)$, its tail part strays away from the fitting line. As we explained in Fig. 1k and Fig. 1i, the straying of the $P(\Delta r')$ is the result of the direct transport of the vesicles from

microtubule-based motors and DDAM. Based on the above understanding, we proposed that the dynamics of the ciliary cargo vesicles contain a fast-active transport motion (directed motion, DM) and a slow active transport blend Brownian motion (anomalous diffusion, AD).

Our modeling of the dynamics of the cargo vesicles thus started from segmentation of the trajectories into DM fragments and AD fragments (Fig. 4b).

For the DM fragments, their instantaneous displacement:

$P(\Delta r)_{dm} = M\tau$, and their instantaneous velocity in the duration $\tau = 4$ s:

$P(\Delta v)_{dm} = M$. We plotted the $P(\Delta v)_{dm}$ (red circles) in Fig. 4d, and we fitted the $P(\Delta v)_{dm}$ with Gaussian distribution, and we obtained the μ_{dm} and σ_{dm} from the plot of $P(\Delta v)_{dm}$.

For the AD fragments, their instantaneous displacement:

$P(\Delta r)_{ad} = \frac{1}{\sqrt{4D\tau}} e^{-\sqrt{2} \frac{\Delta r}{\sqrt{2D\tau}}}$, and their instantaneous velocity in the duration $\tau = 4$ s:

$P(\Delta v)_{ad} = \frac{1}{\tau\sqrt{4D\tau}} e^{-\sqrt{2} \frac{\Delta r}{\sqrt{2D\tau}}}$. We plotted the $P(\Delta v)_{ad}$ (blue circles) in Fig. 4d, and we fitted the $P(\Delta v)_{ad}$ with exponential distribution $P(\Delta v)_{ad} = \beta \exp(-\alpha|\Delta r'|)$, and we obtained the β and α from the plot of $P(\Delta v)_{ad}$.

We defined the ratio of the DM fragments in all trajectories as κ , the DM and AD switch model will generate $P(\Delta v)$ as:

$$P(\Delta v) = \begin{cases} M & w.p.\kappa \\ \frac{1}{\tau\sqrt{4D\tau}} e^{-\sqrt{2} \frac{\Delta x}{\sqrt{2D\tau}}} & w.p.1-\kappa \end{cases} \text{ which is equal to}$$

$$P(\Delta v) = \kappa \frac{1}{\sqrt{2\pi\sigma_{dm}^2}} e^{-\frac{(x-\mu_{dm})^2}{2\sigma_{dm}^2}} + (1-\kappa)\beta \exp(-\alpha|\Delta r'|), \kappa \in [0,1].$$

We estimated the probability κ using a Maximum-likelihood estimation (MLE) in MATLAB and obtained the fitting curve in a green line to fit the PDF of the instantaneous velocity of all the trajectories (green circles, Fig. 4d). To estimate whether the repulsion from DDAM was increased in the calcium signaling, it is critical to calculate the ratio of the active motion in the whole

trajectory. We have shown the fitting results for trajectories in the same color code in Extended Data Fig. 5 for two cells as additional example as shown in Fig.4.

Supplemental Information Reference

- 1 He, W. *et al.* Dynamic heterogeneity and non-Gaussian statistics for acetylcholine receptors on live cell membrane. *Nature Communications* **7**, 11701, doi:10.1038/ncomms11701 <https://www.nature.com/articles/ncomms11701#supplementary-information> (2016).
- 2 Holcman, D. *et al.* Single particle trajectories reveal active endoplasmic reticulum luminal flow. *Nature Cell Biology* **20**, 1118-1125, doi:10.1038/s41556-018-0192-2 (2018).